Modeling precursory laboratory seismicity using a wear-based rate- and state-dependent friction model

P. A. Selvadurai [1], P. Galvez[2], P. M. Mai[2], S. D. Glaser[3],S. Wiemer[1]

[1]Swiss Seismological Service, ETH Zurich, Zurich, Switzerland
[2]King Abdullah University of Science and Technology, Thuwal, Saudi Arabia
[3]Civil and Environmental Engineering, University of California, Berkeley, California, USA

Key Points:

- Rate and state friction models prescribed D_c based on roughness measurements that displayed clear signs of wear
- Polished sections initiated seismicity and controlled stick-slip-dominant to creep-dominant behaviors
- A dominant "mirror" section was found to control foreshocks and possessed the potential to ignite runaway rupture

Corresponding author: Paul Selvadurai, paul.selvadurai@sed.ethz.ch

Abstract

We develop a rate- and state-dependent friction (RSF) model to investigate a compendium of recent experiments performed in the laboratory. In the documented experiments, a fault was sheared until macroscopic stick-slip frictional failure. Before macro-failure, small precursor seismicity nucleated from regions that also experienced aseismic slow slip. This behavior requires heterogeneity and is defined in our model as local variation in frictional parameters inferred from the roughness. During sliding wear introduced a smooth-polished surface onto a previously rough surface and was quantified using a bimodal Gaussian distribution of surface heights. We used spatial distribution of the smooth and rough sections to impose binary partitioning in critical slip distance D_c to a planar frictional model. Simulations revealed that local seismicity nucleated on the "smooth" sections, while the larger "rough" section hosted aseismic slip. As the level of heterogeneity between smooth and rough sections increased, the model transitioned from a predominantly stick-slip to creeping. The simulations produced a dominant asperity, which appeared to control aspects of rupture nucleation: (i) weak heterogeneity caused the dominant asperity to generate foreshocks but also "ignite" cascade-up fault-wide event, while (ii) strong heterogeneity led to constrained repeaters. Seismic source properties: average slip δ, seismic moment M_0, stress drop $\Delta\tau$ and fracture energy $G^{'}$, were determined for each event and agreed with separate kinematic estimates made independently from seismic measurements. Our numerical calculations provide insight into rate-dependent cascade-up nucleation theory where frictional heterogeneity here was associated with wear of solid frictional contacts in the laboratory.

Keywords: Earthquake nucleation, foreshocks, laboratory experiments, rate and state friction, wear, asperities, seismic source properties

Plain Language Summary

Recent seismic observations show that faults experience a range of slip patterns spanning many scales in both space and time. From faults that can creep slowly to those that slip suddenly and release large amounts of energy. Understanding how large and small faults unlock require us to develop models that can produce a range of behavior and characteristics.

Foreshocks are observed in regions that have been found to host large devastating earthquakes but are not well understood. Understanding when, where and how foreshocks appear,

in relation to its mainshock, surrounds the study of earthquake nucleation. Heterogeneity is believed to be a necessary ingredient for foreshocks to occur.

We developed a model to explain laboratory experiments that noticed wearing (polishing) of fault surfaces that also produced foreshocks. Our model used the mirror-finished sections to impose spatial heterogeneity and investigated how varying its properties controlled the faults response. We captured a range of typical seismic behaviors from repeating earthquakes, to foreshocks, to earthquakes that originated at very small scales and possessed the potential to ignite and cascade-up into large system wide events.

1 Introduction

Seismologic observations have captured a growing diversity in slip behavior along natural faults. Observations, such as spatio-temporal variations in seismicity rates (Tormann et al., 2014, 2015; Gulia et al., 2016; Gulia & Wiemer, 2019), the presence of repeaters in aseismically creeping fault sections (e.g. Nadeau et al., 1994; Nadeau & McEvilly, 1999; Shirzaei & Bürgmann, 2013; Uchida, 2019), variations of slow slip distribution over large scales inferred from geodetic measurement (e.g. Brodsky & Lay, 2014; Ruiz et al., 2014; Socquet et al., 2017), the earthquake potential on sections prone to large ruptures (Bürgmann et al., 2000; Bürgmann, 2004), the observed variability in spatio-temporal slip patterns during rapid rupture (e.g. Mai & Beroza, 2002; Tinti et al., 2005; Dreger et al., 2007; Galvez et al., 2016; Mai et al., 2018) suggest that coupling of faults and the ability to resist frictional breakdown is heterogeneous.

Heterogeneity in frictional properties is also necessary to explain the observation that, in certain cases, precursory seismicity has been detected in regions that also support the steady growth of a preslip region (A. Kato et al., 2012, 2016; Obara & Kato, 2016; Ruiz et al., 2014; Bouchon et al., 2013; Bürgmann, 2004). Preslip is a slow accumulation of fault slip in a region that grows outwards to a critical size where it becomes unstable and the mainshock ensues (Mogi, 1985; Ohnaka, 1992; Ben-Zion, 2008). This portion of the seismogenic cycle is known as the nucleation phase. This behavior has been identified from the onset of the mainshock's seismogram (Iio, 1995; Ellsworth & Beroza, 1995; Beroza & Ellsworth, 1996), whilst recent improvements in geodetic measurements help to lower the detectable threshold and identify the nucleation phase over long time scales (months to years) and length scales (kms) (e.g., Roeloffs, 2006; Wang & Bilek, 2014; Ruiz et al., 2014;

Socquet et al., 2017). In certain cases, precursory seismicity in the form of foreshocks has been observed prior to the mainshock (e.g., Dodge et al., 1995, 1996; Bouchon et al., 2011). While it is unclear if all mainshocks are preceded by foreshocks (Brodsky & Lay, 2014; Mignan, 2014; Seif et al., 2018) they are currently only identifiable in retrospective analysis. Due to their forecasting potential, foreshocks have become important phenomena to study.

The study of the spatio-temporal growth of a preslip region and its transition from slow (quasi-static) to fast (dynamic) slip has been well documented in laboratory experiments (Dieterich, 1978; Okubo & Dieterich, 1984; Ohnaka & Shen, 1999; Nielsen et al., 2010; Latour et al., 2013; Fukuyama et al., 2018; Zhuo, Guo, et al., 2018; Ke et al., 2018; Buijze et al., 2020). More recently, along with measuring the spatio-temporal evolution of a slow preslip region, acoustic emission sensors were deployed to detect localized, high-frequency and impulsive events that spontaneously emanate from sections of the fault that also hosted the preslip region (Ma et al., 2002; McLaskey & Kilgore, 2013; McLaskey & Lockner, 2014; Selvadurai & Glaser, 2015a; Passelègue et al., 2017; Zhuo, Liu, et al., 2018). Analysis of these localized events using seismological models found the moment released with respect to their geometry scaled with earthquakes in nature (McLaskey et al., 2014; Selvadurai, 2019). This similarity has sparked more interest in understanding the implications that laboratory foreshocks have on the growth and stability of the preslip region and the influence of foreshocks themselves on the size and timing of the larger mainshock (McLaskey, 2019).

A major question is when does a foreshocks 'cascade-up' into the mainshock? Studies of the initial onset of seismic rupture using seismograms suggest that asperities exist at many spatial scales, and that the triggering of a cascading-style failure mechanism might stem from failure of a smaller section (Okuda & Ide, 2018a; Ide, 2019). This type of hierarchical breakdown may indicate the existence of a hierarchical plate interface structure (Ide & Aochi, 2005; Aochi & Ide, 2014, 2017). Foreshocks might be local failures of these asperities that do not fully 'cascade-up' but possess 'runaway potential' if conditions are favourable.

Conditions that controls the occurrence of foreshocks (or other types of precursory seismicity) during the nucleation phase, even at laboratory scales, is not entirely clear. In previous laboratory foreshocks studies (McLaskey & Kilgore, 2013; Selvadurai & Glaser, 2015a), frictional fault behavior was dictated by a dry and gouge-free fault environment. In these cases, heterogeneity is believed to occur because of geometric interaction between two rough surfaces that give rise to contact asperities with locally high normal stresses. The

contact heterogeneity was confirmed by Selvadurai and Glaser (2017) with measurement of spatially variable normal stress determined from a pressure sensitive film placed along the interface; this has also been widely investigated in the field of statistical contact mechanics (e.g. Greenwood & Williamson, 1966; Johnson, 1985; Persson, 2006).

The relationship between contact heterogeneity and mechanisms explaining spontaneous occurrence of foreshocks in sections of accumulating slip were examined. Selvadurai and Glaser (2017) proposed that localized precursory events occurred on asperities that exhibit higher levels of normal stress, thus locally decreasing its critical nucleation length scale (defined later in Section 2.1). If the asperity was geometrically large enough with locally high normal stress, favorable conditions allowing for the spontaneous localization of foreshocks could occur in the preslip region. This hypothesis is also discussed by McLaskey (2019). Another mechanism proposed by McLaskey and Kilgore (2013) was that the increased stressing rate around the local geometric interference between surfaces might contribute to higher shear stresses resulting in the dynamic failure of these contact asperities.

But why do the foreshocks arrest? What type/level of frictional heterogeneity is necessary to arrest the rupture that should, on a homogeneous interface, continue to rupture over the entire frictional interface? From the study of dynamic rupture propagation, after spontaneous initiation of dynamic rupture, the slip front begins to expand in a crack-like manner, accelerating outwards to a critical velocity, whereby it may transition to a pulse-like dynamic rupture (Heaton, 1990; Meier et al., 2016). Experiments and numerical investigations into the causes of complex rapid rupture nucleation and arrest in the laboratory are highly dependent on the stress states on the fault ahead of the rupture (Rubinstein et al., 2004, 2006; Ben-David et al., 2010; Svetlizky & Fineberg, 2014; Fineberg & Bouchbinder, 2015; Maegawa et al., 2010; Trømborg et al., 2011; Kammer et al., 2012; ?, ?; Kammer et al., 2015) and appear to control even slower quasi-static ruptures (Selvadurai et al., 2017). The study of why/how laboratory ruptures arrest in these studies are performed at larger scales and do not study the high-frequency emissions measured using acoustic emission sensors. For this reason, it becomes difficult to investigate the interaction of the foreshock/nucleation region which requires, in the laboratory, a broadband temporal and spatial understanding of slip: from frequencies ranging from DC to $\sim$ 1.5 MHz and length scales ranging from tens of microns to meters.

In this study, we aim to understand mechanisms for localized fast ruptures embedded within a slow rupture where asperities are formed from geometric mismatch of the two rough surfaces. We apply a numerical rate- and state-friction (RSF) model (Dieterich, 1979; Ampuero & Rubin, 2008; Rubin & Ampuero, 2005) to explain a compendium of laboratory data from a specific direct shear friction experiment performed on a fault analog. The observations follow recent publications the reader may consult for experimental details,

1. Selvadurai and Glaser (2015a) looked at the nucleation phase where a slow preslip front was observed prior to onset of system wide stick-slip instabilities. Within this preslip region, localized foreshocks were observed;
2. Selvadurai and Glaser (2017) investigated characteristics of the roughness and quantitative analysis of the contact stresses on the asperities were documented;
3. Selvadurai (2019) estimated seismic source properties of the localized foreshocks events that occurred in the preslip nucleation region were quantified using kinematic source models.

1.1 Summarized Experiment

A schematic diagram of the direct shear friction apparatus is presented in Figure 1(a). We refer to this scale as the macrosopic scale for the discussion. Experiments consisted of loading a long slender polymethyl methacrylate (PMMA) slider onto a larger PMMA base plate; the interacting faces were first sandblasted. During an experiment, the fault was maintained under constant normal load F_n. The top slider was driven at a constant macroscopic loading rate V_{LP} and an in-line shear load cell was used to measure the bulk frictional resistance F_S along the fault (see Figure 1(b)).

In Figure 1(b) the slip evolution (black line) for the stick-slip event as measured by the non-contact eddy current sensor (NC5). Figure 1(c) depicts a schematic representation of the eddy current sensor (mounted on the base plate) and the wing target attached to the slider block $\sim$ 2.5 mm above the interface. The inductive eddy current sensors measured slip δ in the x-direction. We refer to this scale as the mesosopic scale for the discussion.

During a stick-slip cycle, the slow and smooth accumulation of aseismic slip is detailed in Figure 1(d); lines of constant slip rate (magenta) are superimposed over the slip evolution curve. The fault displayed an acceleration of aseismic slip leading to the stick-slip event. This

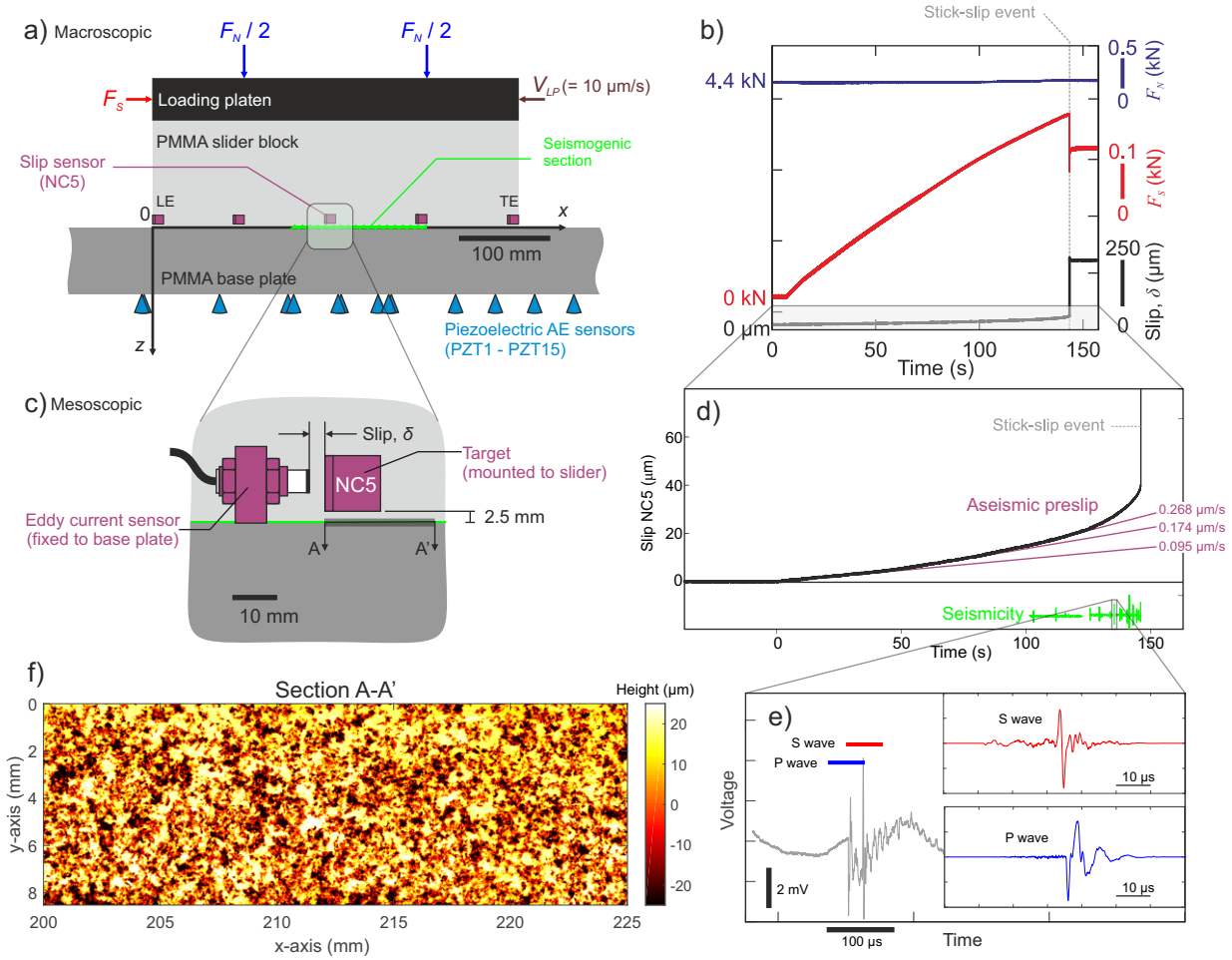

Figure 1. **(a)** Schematic details of the direct shear friction apparatus depicting the general loading conditions and sensor placements are displayed. For more technical details please consult Selvadurai and Glaser (2015b). **(b)** Typical result demonstrating the bulk frictional evolution in terms of shear slip and shear force leading up to failure. **(c)** Schematic details of the non-contact eddy current sensor placement at the mesoscopic scale. **(d)** Detailed slip measurement during the experiment presented in (b). Mesoscopic slow aseismic slip was observed prior to macroscopic stick-slip failure. Lines of constant slip velocity are displayed for reference. Seismicity (green) is represented schematically to document presence of local fast slip as the accelerated aseismic slip was observed. **(e)** Example of precursory seismicity recorded using PZT7. Seismicity showed clear P and S wave arrivals. More detailed source analysis has been performed by Selvadurai (2019). **(f)** Surface roughness measurement taken *a posteriori* using the longer length scale optical profilometer (Selvadurai & Glaser, 2017). The region on the fault associated with this scan is highlighted by the cross-section A-A' in (c).

type of observation is fairly common in laboratory friction experiments. However, we also observed pronounced impulsive events, detected using an array of calibrated piezoelectric transducers (PZT) that measure high-frequency vibrations (100kHz to 1500 kHz) produced by seismic stress waves. Seismicity is represented schematically (green) since the time scales between the slow slip and this impulsive source were $\sim$ 6 orders of magnitude different. Figure 1(e) depicts isolated P and S waves from a typical impulsive source measured by PZT7 (Selvadurai, 2019).

Our friction model requires spatial heterogeneity to explain the observations of synchronous and concomitant slow (Figure 1(d)) and fast rupture (Figure 1(e)). In our RSF model we base spatial heterogeneity on the experimental *a posteriori* measurement of surface roughness. Figure 1(f) presents the optical scan of surface roughness on the top slider block surface through the cross-section A-A' in Figure 1(c). The scan was taken below the non-contact sensor NC5.

1.2 Surface Roughness Analysis

Roughness has been proposed as a controlling feature linked to variability in frictional behavior on faults (Scholz & Aviles, 1986; Scholz, 2002). Studies of the roughness of large exposed outcrops have been used to develop models describing the heterogeneity in stress and strength on active faults (e.g., Schmittbuhl et al., 2006). Large sections of exposed faults exhibit variability in roughness, which can be characterized using various measurements techniques (Power & Tullis, 1991; Schmittbuhl et al., 1995; Renard et al., 2006; Candela et al., 2009; Brodsky et al., 2011; Siman-Tov et al., 2013; Kirkpatrick & Brodsky, 2014; Candela & Brodsky, 2016; Brodsky et al., 2016). We briefly describe methods used to quantify surface roughness in the fields of contact mechanics, tribology and geophysics that we will then use to characterize the interface presented in Figure 1(f). We measure average roughness as the root mean square:

$$h_{rms} = \sqrt{\left(\frac{1}{N}\right)\sum_{i=1}^{N} h_i^2}, \tag{1}$$

where N is the total number of measurement points and h_i is the individual surface height. To estimate statistical properties of surface heights we also employ the probability density functions (PDFs) of the surface height h defined by a Gaussian distribution, given as follows:

$$\phi(h) = (2\pi\sigma^*)\, exp\left[\frac{(h-\mu^*)^2}{2\sigma^{*2}}\right], \tag{2}$$

where μ^* is the arithmetic mean and σ^* is the standard deviation. Building on equation eq1 the PDF for a bimodal Gaussian mixture model is given by

$$\Phi(h) = p \cdot \phi_1(h) + (1-p) \cdot \phi_2(h), \tag{3}$$

where p is the mixture ratio between the two Gaussian distribution functions ϕ_1 and ϕ_2, each with their individual means and standard deviations. When fitting eq1 and eq2 to the experimental measurements we employ a maximum likelihood estimation (MLE) of the means, standard deviations and mixture ratio.

Finally, we estimate surface properties using power spectral density (PSD), i.e. the square of the modulus of the normalized Fourier transform, of a self-affine surface profile following

$$P(k) \propto k^{-(1+2H)}, \tag{4}$$

where k is the wavenumber and H is the self-affine scaling exponent or Hurst exponent (Power & Tullis, 1991; Schmittbuhl et al., 1995; Mai & Beroza, 2002; Candela et al., 2009). By plotting equation eq999 we can estimate H using linear regression of log-log slope of the relationship between the PSD and wavenumber $\beta = -(1+2H)$.

1.3 Evidence of fault wear

The facilities and measurement techniques are discussed in detail by Selvadurai and Glaser (2017). Figure 2(a) displays estimates of surface roughness using the root mean square (16.7 μm using equation eq99), Gaussian (equation eq1) and bimodal Gaussian (equation eq2) distributions for the surface presented in Figure 1(f). The values of the means (μ^*), standard deviations (σ^*) and mixture ratio (p), are given for the modal (magenta) and bimodal (cyan), models with units of μm. The shape of the distribution is most adequately characterized by the bimodal Gaussian distribution. Evolution of roughness from Gaussian to bimodal Gaussian can be quantified using the polish-rate decay (wear decay or *Borucki* wear) function (Adachi & Kato, 2000; L. Borucki, 2002; L. J. Borucki

et al., 2004; Ciavarella, 2016; He et al., 2017; Hu et al., 2019a). This type of distribution has been well-documented in the field of tribology and is used to characterize wear of the interface. As the surface wears from a Gaussian to bimodal Gaussian it reaches a steady state roughness. This worn characteristic was likely due to the lapping procedure described in Selvadurai and Glaser (2015a) in which $\sim$ 36.1 mm slip was used to precondition the originally sandblasted surface before any experiments were reported. We see that wear had produced a smoother surface (i.e. the 'tail' in the PDF), and this polished surface existed within the encompassing rougher surface.

Figure 2(b) marks the Hurst exponent estimated using the power spectral density from the surface roughness transects in the $x-$direction. The average PSD was used to estimate a Hurst exponent $H = 0.43$ between the wavenumbers of 1 mm $^{-1} < k <$ 50 mm $^{-1}$ from equation eq999. We note that any deviations of the values presented here from those in Selvadurai and Glaser (2017) are due to the more accurate cropping of the measurement region presented in Figure 1(f).

Figure 2(c) reveals a raw photograph of the surface of the seismogenic section of the fault (Selvadurai & Glaser, 2017), revealing polished spots with a "mirror-like" finish that was responsible for the tail in the PDF of the surface roughness. From Selvadurai and Glaser (2017), the polished surface 'mirrors' were 188 times smoother than the overall RMS roughness for the full region ($h_{RMS} = 16.\ 7\ \mu$m). Figure 2(d) highlights the darker regions by converting the raw image from RGB to light intensity between the range of $0 < I <$ 0.35 (Gonzalez et al., 2009). The inset image displays the complexity associated within the polished section.

The presence of fault-mirrors (FM) observed on natural outcrops have sparked interest from the geophysical community (Fondriest et al., 2013; Kirkpatrick et al., 2013; Siman-Tov et al., 2013). Laboratory experiments have been crucial in understanding the mechanism surrounding the formation of FMs and the debate of whether the presence of a fault mirror can be used as an indicator of seismic slip (Fondriest et al., 2013; Siman-Tov et al., 2013; Pozzi et al., 2018), but they have also been reproduced during slow slip (Tisato et al., 2012; Siman-Tov et al., 2015), in high-temperature environments (Pluymakers & Røyne, 2017) and observed along glacial boundaries (Siman-Tov et al., 2017). Figures 2(e) and (f) show fault mirrors on the Dead Sea Transform and the Corona Heights Fault (USA), respectively, that formed at different scales. Goldberg et al. (2016) believe that these FMs

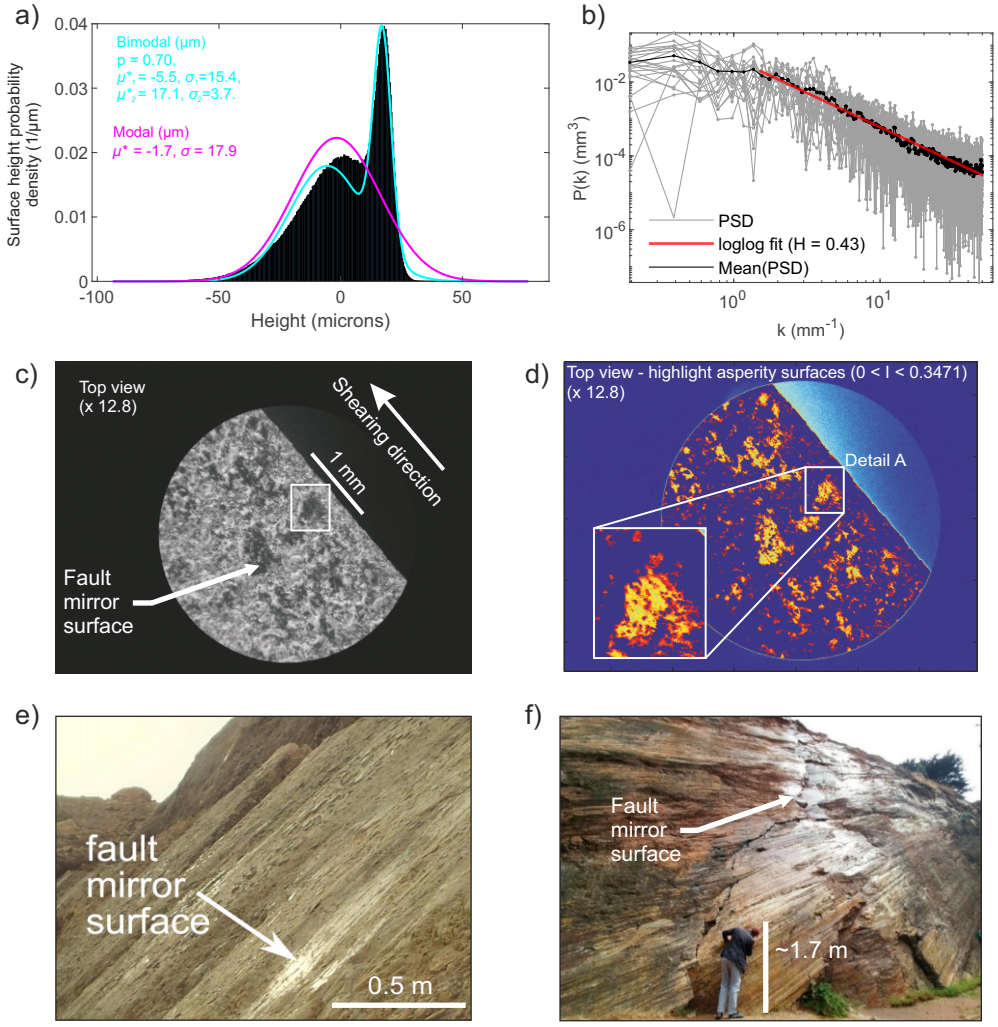

Figure 2. **(a)** Surface height probability density function for the surface in Figure 1(f). Values of three surface roughness models are established for the root mean square (black), Gaussian (magenta) and bimodal Gaussian (cyan) – the values are given in μm. **(b)** Estimate of the Hurst exponent from the same surface are estimated from the power spectral density (PSD) described by equation eq999 along the all transects in the $x-$direction (gray lines). The mean PSD for this surface is displayed in black and the Hurst exponent $H = 0.43$ (red line) was estimated. **(c)** Image of the worn PMMA fault surface from (Selvadurai, 2015) reveals dark, smooth spots that are indicative of worn sections of the PMMA slider block. **(d)** Post-processing highlights the darker smooth sections. The inset image displays the spatial complexity of the smooth region. **(e)** Exposed outcrop with a mirror surface on a fault located along the Dead Sea Transform (image adapted from Goldberg et al. (2016)). **(f)** Exposed outcrop with striated, glossy surface of the Corona Heights Fault (USA) (adapted from Verberne et al. (2019)).

can potentially promote seismicity and can form at lower slip rates than previously thought (Verberne et al., 2019). While there are differences between the mechanisms controlling how surfaces polish and FMs develop on rock-rock interfaces in hydro-thermal environments and controlling their development on a plastic PMMA surface (Bouissou et al., 1998), we are more interested in how the initial conditions of a "smoother surface embedded in a rougher fault" affect the frictional dynamics associated with using a RSF model.

2 Rate- and state-dependent (RSF) friction model

2.1 Theory

The RSF constitutive friction law is phenomenological and derived from laboratory experiments (Dieterich, 1979; Ruina, 1983). The model describes the behavior of a fault's resistance to sliding in terms of shear stress τ as a function of slip rate V and state variable θ. This is given as:

$$\tau\left(V,\theta\right)=\sigma_n\left[\mu+a\ln\frac{V}{V^*}+b\ln\frac{V^*\theta}{D_c}\right], \tag{5}$$

where σ_n is the normal stress, μ is the reference steady-state friction coefficient at an arbitrary reference slip rate V^*, D_c is the characteristic slip distance and a and b are constitutive parameters describing the direct and evolution effects, respectively. We adopt the state parameter in the form of the so-called "slip law" because of to its ability to model recent laboratory studies (Bhattacharya et al., 2015; Kaneko & Ampuero, 2011; Kaneko et al., 2016):

$$\dot{\theta}=-\frac{V\theta}{D_c}\ln\frac{V\theta}{D_c}, \tag{6}$$

where friction at steady state ($\dot{\theta}=0$) is given as

$$\tau_{ss}\left(V\right)=\sigma_n\left[\mu+(a-b)\ln\frac{V}{V^*}\right]. \tag{7}$$

From equation eq7 we see that constitutive parameters $(a-b)$ play an influential role in how the interface behaves at steady-state. For $(a-b)<0$, τ_{ss} will decrease as slip rate V increases. A fault with these characteristics is known as velocity-weakening (VW) and is prone to spontaneous instability if the fault stiffness is below a critical stiffness. Stiffness

of the VW spring-slider system was investigated by Ranjith and Rice (1999) who found the critical stiffness to be:

$$k_{cr} = \frac{\sigma_n (b-a)}{D_c}. \tag{8}$$

This implies that quasi-static steady-state slip is stable ($V \to V^*$) or unstable ($V \to \infty$) if the spring stiffness is greater than or less than the critical value k_{cr}, respectively. Fault stiffness is inversely proportional to the minimum half-length of a nucleation zone capable of instability:

$$L_c = \eta \frac{G^* D_c}{\sigma_n (b-a)}, \tag{9}$$

where $\eta = (7\sqrt{2})/(3\pi)$ (Dieterich, 1992) for a square patch, the corrected shear modulus $G^* (= G/(1-\nu))$ was employed due to the Mode II plane strain conditions and ν is the Poisson's ratio.

The equation of motion controlling slip on a planar fault is given by:

$$\tau_{el}(\mathbf{x}) - \tau(\mathbf{x}) = \frac{G^*}{2V_S} V(\mathbf{x}), \tag{10}$$

where τ_{el} is the elastostatic shear stress due to the loading boundary condition (Horowitz & Ruina, 1989). The inertial term on the right hand side represents the radiation damping term for S waves produced along the fault at point $\mathbf{x}$, which expands at speeds closer to the shear wave speed V_S of the material (Rice, 1993).

Quasi-static interactions between fault elements are calculated using the boundary element method (BEM) and all calculations reported in this study were solved using a Quasi-DYNamic earthquake simulator (Luo et al., 2017). QDYN is a boundary element software designed to simulate earthquake cycles (seismic and aseismic slip on tectonic faults) under the quasi-dynamic approximation (quasi-static elasticity combined with radiation damping) on faults governed by RSF and embedded in elastic media. Solution convergence and mesh discretization of the heterogeneous models described later is given in Supplemental Methods S1.

Dieterich (1992) showed that RSF combined with elasticity leads to the common length scale

$$L_b \equiv \frac{G^* D_c}{\sigma b}. \tag{11}$$

This characteristic dimension was later theoretically confirmed by Rubin and Ampuero (2005) and controls aspects of earthquake nucleation and the transition from aseismic to seismic behaviour. We define this transition threshold to be:

$$V_{dyn} = \frac{2aV_s}{G^*}, \tag{12}$$

which represents the transition point where the inertial term in equation eq8a becomes significant.

2.2 Recent advances in RSF modeling from the laboratory

Experiments performed by Nielsen et al. (2010) and Latour et al. (2013) have benefited from increasing the fault's compliance using analog materials (glassy polymers) in frictional tests. These experiments benefit from improved spatio-temporal measurement of slip was achieved by using high speed digital cameras. Increased refinement in both spatial and temporal measurements clearly showed the so-called "preslip" or nucleation zone. This nucleation region was predicted in RS models (Dieterich, 1992; Rubin & Ampuero, 2005; Ampuero & Rubin, 2008) but was difficult to show with high spatial resolution before novel sensing techniques.

Modeling efforts by Kaneko and Ampuero (2011) and Kaneko et al. (2016) showed that frictional behavior of the 'plastic-on-plastic' sliding experiments can be explained using RS friction models. These models are informative and promote the idea of a 'smooth transition' of frictional sliding over the macroscopic length scale of the experimental fault. It explained both the spatial and temporal evolution of observed nucleation features of those laboratory ruptures. While these studies have demonstrated RSF ability to explain complex transients, neither addressed the role of fault roughness; they assumed this is embedded implicitly in the phenomenological nature of the RSF parameters.

Roughness has been established to affect dynamic rupture propagation (e.g. Dunham et al., 2011; Fang & Dunham, 2013), nucleation physics (e.g. Tal et al., 2018) and the presence of aseismic transients (Ozawa et al., 2019). In these studies the fault is considered to be perfectly mated and roughness is described using the Hurst exponent. As the level of fault matedness in the modeled experiments was unclear at any time, we chose to use a *cutting plane method* that spatially discretizes the frictional properties applied on a planar fault by using measurements inferred from the two (smooth and rough) surfaces defined by bimodal Gaussian model described before.

2.3 Cutting plane method

The *cutting plane method* splits the roughness into two separate sections: smooth and rough. Using this method we assign binary sets of frictional parameters to both the smooth and rough regions of the roughness profile. A 'cutting plane' was defined to be exactly between the two means of the bimodal distributions that was formed due to wear. In this study, we build a simple 1-D model and arbitrarily choose the transect of the rough surface at $y = 2$ mm. Figure 3(a) displays the roughness along x at y= 2 mm (black line). In Figure 3(a), (b) and (c) the cutting plane (red) was defined as $h_{cut} = (\mu_1^* + \mu_2^*)/2 = 12.54$ μm using the bimodal Gaussian parameters calculated for surface heights along transect at $y = 2$mm. Figure 3(b) depicts the probability distribution of the surface heights from the sample transect and the cutting plane in red. We assume that the "smooth" surface is the"upper" one (above the cutting plane) that is characterized more effectively by the Gaussian distribution with lower standard deviation (σ^*), whereas the "rough" surface was below the cutting plane and had a larger standard deviation.

A scaling function (SF) is used to partition the smooth and rough sections of the fault. Figure 3(c) marks a detailed view of the roughness (black), the cutting plane (red) and the scaling function (blue). When roughness was above the cutting plane the scaling function (SF) was unity. All heights below the cutting plane were prescribed as scaled values. This allowed us to control the magnitude, or 'order', of heterogeneity. For this example, the order was $O = 20$. The SF produced heterogeneity in two ways: (i) spatial variations were controlled by the location where the roughness profile crossed the cutting plane, and (ii) the level (order) of heterogeneity – the peak-to-peak range of SF – was chosen by the modeler. The order of the SF(x) is clearly seen in the PDF in Figure 3(d).

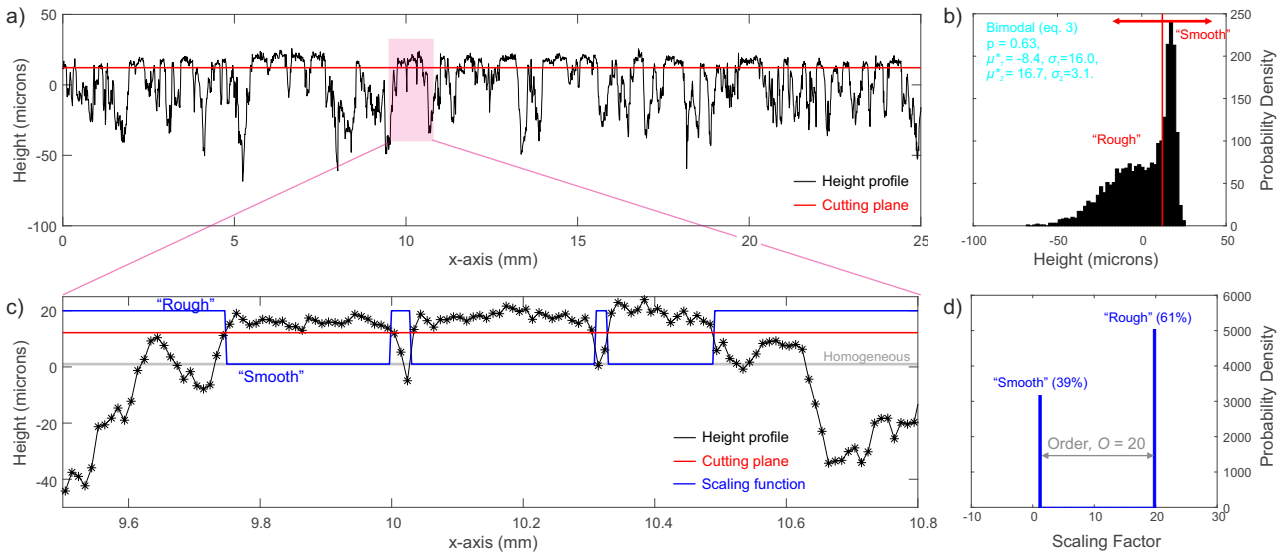

Figure 3. **(a)** 1-D roughness profile (black) taken from the transect at $y = 2$ mm in Figure 1(f). The cutting plane $h_{cut} = 12.54$ μm is used to separate the bimodal distribution into smooth and rough surfaces. **(b)** PDF of the height profile in (a) with the cutting plane (red vertical line). **(c)** Small section of the height distribution showing the roughness profile (black line), the cutting plane (red line) and the scaling function (blue line). **(d)** PDF of the scaling function SF(x) with an order of heterogeneity $O = 20$.

We approach the modeling in a non-traditional manner and imposed heterogeneity primarily through the frictional critical slip-weakening variable $D_c(x)$. Spatial fluctuations in fault roughness – smoother and or rougher sections – assumed properties based on arguments in past laboratory observations (Marone & Cox, 1994). This assumption also follows micro-mechanical simulations governing the critical slip-weakening variable D_c on dry, gouge-free interfaces (Yoshioka & Iwasa, 1996; Yoshioka, 1997). Smooth sections were prescribed lower $D_{c,low}$, whereas rougher sections have a higher level of $D_{c,high}$. Spatial fluctuations in critical slip distance was given the lower value multiplied by the scaling function $D_c(x) = D_{c,low}$·SF(x). The magnitude D_c in the rough sections depended on the order O of the scaling function. For example, for order O=20, the larger critical slip value was $D_{c,high} = \max[D_c(x)] = 25$ nm· $20 = 500$ nm $= 0.5$ μm.

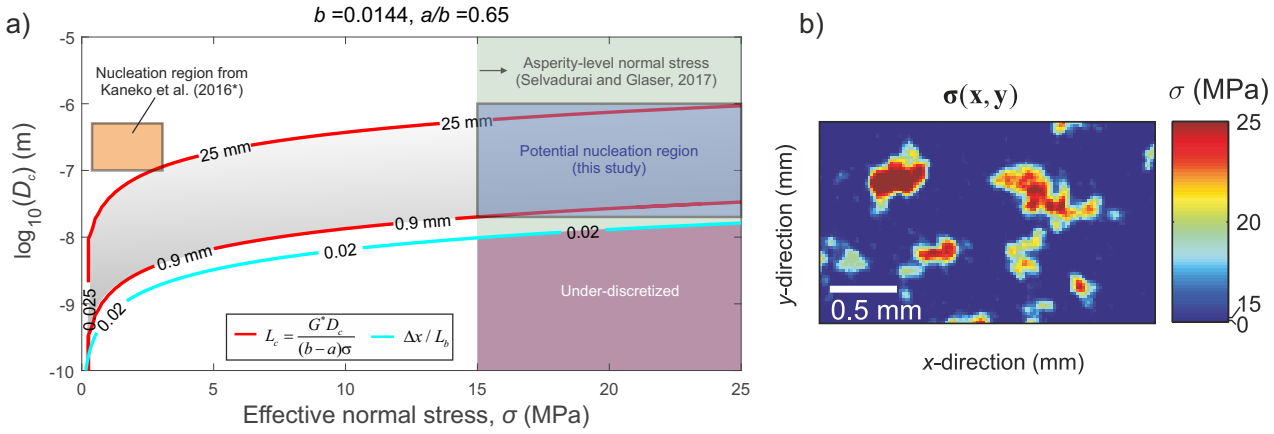

Figure 4. **(a)** Initial estimates of the nucleation parameter space (L_c) based on measurements of local normal stress (Selvadurai & Glaser, 2017), minimum mesh discretization ($\Delta x/L_b$) and maximum critical nucleation size $L_c = 0.025$ m. The gray region represents possible nucleation sizes for the mesoscopic length scale. The orange region represents the ranges of D_c and normal stress σ_n that nucleated full fault rupture in ? (?), $*a/b = 0.6944$]Kaneko2016. **(b)** Example of asperity-level normal stress field measured using an experimental pressure sensitive film (adapted from Selvadurai & Glaser, 2017).

2.4 Frictional parameter space

Although we chose parameters based on our previous studies we also incorporated assumptions from the literature. The goal of our modelling is to identify conditions that produce local seismicity – a critical experimental observation obtained from the PZT sensors. Figure 4 demonstrates how the critical nucleation length L_c (equation eq8) varies with D_c and the normal stress σ_n. Based on experiments performed by Berthoude et al. (1999) for PMMA, we set $a/b = 0.65$ and $b = 0.0144$. For reference, curves representing constant critical nucleation length are marked in red for $L_c = 25$ mm and 0.9 mm.

To further constrain our models, we examined the experimentally measured asperity normal stress from the concerted study of Selvadurai and Glaser (2017). Using the calibrated pressure film (Selvadurai & Glaser, 2015b), they found the asperities attained normal stresses ranging from $\sigma_n = 12$ to 25 MPa. This range of normal stress is superimposed in Figure 4(a), which further bounds the potential nucleation conditions in our RSF model.

Adequate fault meshing for the numerical simulations is needed to correctly capture the dynamic processes at the rupture tip during seismic events. Our calculations were

based on estimates of the cohesive (or breakdown) zone length scale L_b (equation eq8b). We found that to accurately capture local frictional breakdown it was necessary to apply a minimum grid size of $\Delta x/L_b < (1/50)$ was needed for $a/b = 0.65$. In this model we choose to use $2^{13} = 8192$ grid points over the length $L = 25$ mm of the mesoscopic domain, resulting in a resolution $\Delta x \sim 3$ μm. Our domain is much smaller than previous RSF model used to understand laboratory friction experiments. The macroscopic parameter space used by Kaneko et al. (2016) (orange region) to understand the behavior of similar plastic-on-plastic sliding experiment performed by Latour et al. (2013) is given for reference. Table 1 presents baseline frictional, material and length scale parameters used in this study. More information on the convergence tests for the heterogeneous models is given in the Supplemental Information S1.

Table 1. General model parameters used in the 1-D RSF models.

Parameter	**Symbol**	**Value**
Shear modulus	G	2.39 GPa
Poisson ratio	ν	0.32
Shear wave speed	V_S	1330 m s^{-1}
Reference friction coefficient	μ	0.6
Reference slip rate	V^*	0.1 μm s^{-1}
Dynamic sliding threshold	V_{dyn}	0.177 m s^{-1}
Loading plate velocity	V_{LP}	0.1 μm s^{-1}
Lower critical slip distance	$(D_c)_{low}$	25 nm
Heterogeneous critical slip distance	$D_c(x)$	$(D_c)_{low} \cdot$ SF(x)
Normal stress	σ_n	25 MPa
Length of mesoscopic domain	L	25 mm
Height of mesoscopic domain	$H^{'}$	2.5 mm
Width of mesoscopic domain	W	∞
Grid size	Δx	3 μm
Grid points	n	2^{13}
RS parameter b (VW)	b	0.0144
RS parameter a (VW)	a	0.00936
Simulation time	t_{sim}	600 s

3 Computational Results

The general domain for our 1-D frictional model is presented in Figure 5(a). This represents the mesoscopic region under the eddy current target in Figure 1(c). The geometry of the domain is $L = 25$ mm (extent of the roughness measurement in the direction of slip), $H^{'} = 2.5$ mm (height of the material just below the eddy current target) and $W = \infty$ (plane strain conditions). The boundary element code QDYN assumes frictional properties (a, b and D_c) and normal stress (σ_n) at each node on the interface. Figure 5(b) displays a schematic representation of the boundary value problem. A few representative nodes are depicted as slider blocks. Communication between frictional nodes is shown as spring elements. QDYN solves the equation of motion given in eq8a. Before moving to more complex, heterogeneous cases we examine the behavior of the homogeneous case to develop the fundamental understanding of the system and to establish the reference case.

3.1 Homogeneous case

From the mesoscopic geometry we build the 1-D homogeneous model, expressed schematically in Figure 5(b). For the homogeneous case, each node has velocity-weakening (VW) conditions $(a - b)$ = -0.005, $a/b = 0.65$, normal stress $\sigma_n = 25$ MPa and a critical slip-weakening distance $D_c = 25$ nm. For the homogeneous case, the steady-state sliding velocity V^* was assumed to be equal to the load point velocity V_{LP}. We were able to determine this experimentally from the near-fault slip velocity measurements made using the eddy current slip sensors displayed in Figure 1(d); $V_{LP} = 0.1$ μm/s was used in this study.

Each numerical simulation lasted for $t_{sim} = 600$ s, which allowed the fault to fully-develop a periodic stick-slip response (Hillers et al., 2007). Figure 5(c) and (d) show a short time window (500 to 600 s) of the slip velocity and shear stress, respectively, averaged over all nodes in the model. We see that periodic ruptures are analogous to a 'stick-slip' event. Over the full simulation, 18 full rupture stick-slip events were recorded for the homogeneous case but only three are displayed here. Coseismic slip was defined when any node experienced a sliding velocity $V > V_{dyn}$ =0.177 m/s defined by equation eq8c. To further characterize the homogeneous case, Figure 5(e) reveals the relationship between average slip velocity and shear stress, which depicts the seismogenic evolution of the systems between different seismic regimes: interseismic, preseismic, coseismic and postseismic (Ampuero & Rubin, 2008).

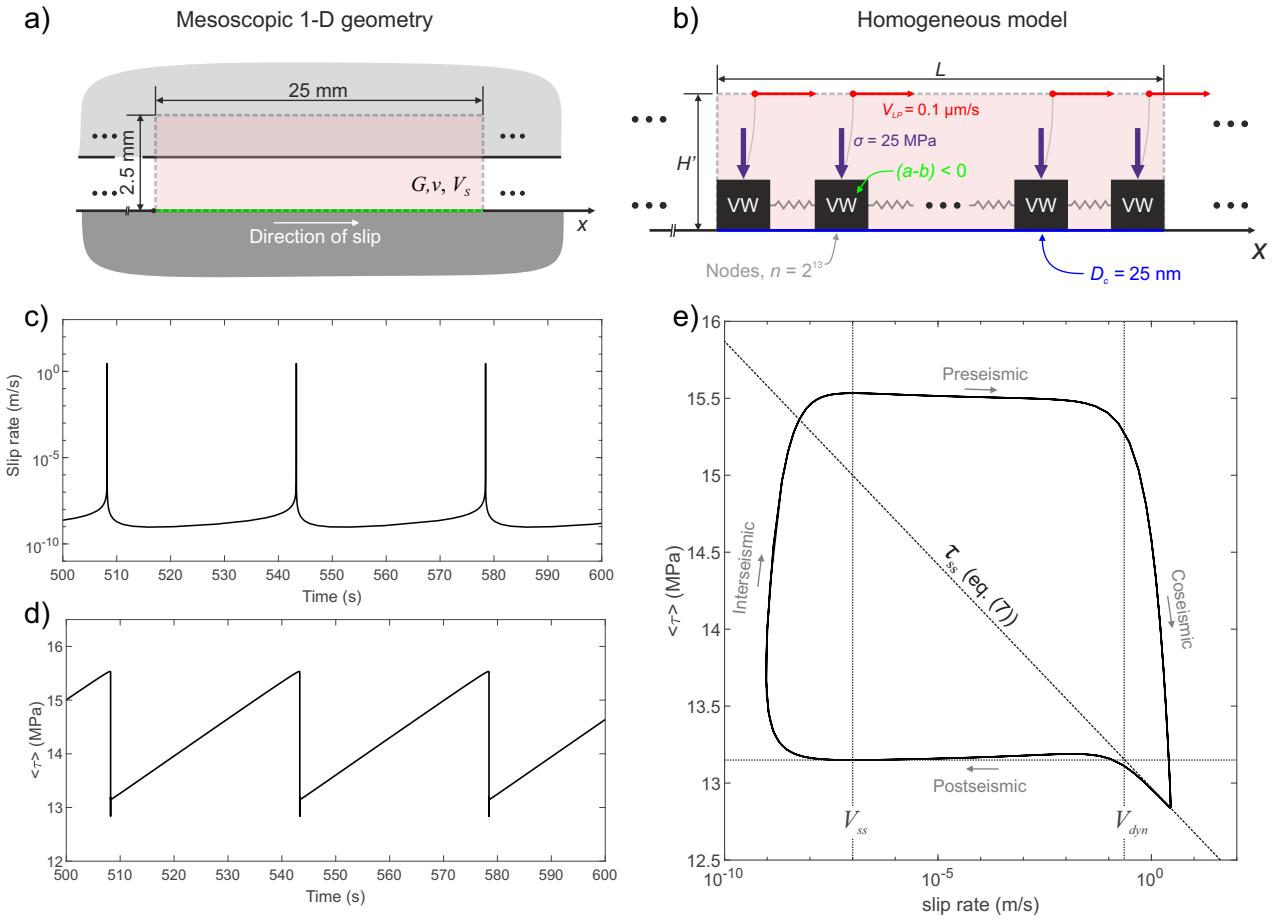

Figure 5. **(a)** General dimensions of the model domain in Figure 1(c). **(b)** Description of the 1-D boundary value problem being solved by QDYN. RS frictional behavior is described by equations eq5 to eq8. **(c)** Average slip velocity and **(d)** average shear stress along the fault for t_{sim} between 500 to 600s. We see that the fault underwent stick-slip behavior. **(e)** A diagram of the earthquake cycle for the VW fault that includes preseismic, coseismic, postseismic and interseismic phases.

3.2 Heterogeneous D_c-model

We produce heterogeneity by varying the distribution of the critical slip weakening distance D_c according to the scaling function (SF) in Figure 3(c). The D_c-model shares some properties of the homogeneous case ($b = 0.0144$, $a/b = 0.65$, $\sigma_n = 25$ MPa) and is depicted schematically in Figure 6(a). For the D_c-model we prescribe the lower value of critical slip weakening distance $D_{c,low} = 25$ nm. Using the scaling function from the cutting plane method, we can capture the spatial variation in the critical slip weakening distance given as $D_c(x) = D_{c,low} \cdot \mathrm{SF}(x)$. Figure 6(b) reveals the spatial fluctuations in $D_c(x)$ for heterogeneity on the order of O20. For reference, the spatial distribution of the homogeneous properties are given in Figure 6(c).

The average slip rate and shear stress for this D_c-model (O20) are marked in blue in Figures 6(d) and (e), respectively. For reference, we also depict the results from the homogeneous model O1 (black). We see that the fault experienced stick-slip behavior – the small spikes in slip velocity – but did not experience full rupture with a large drop in shear stress drop as in the homogeneous case.

Next we investigated the effect of different levels of heterogeneity. In Figure 7 the average fault behavior is depicted for three levels, O10 (red), O15 (green) and O20 (blue), that all use the same scaling function $\mathrm{SF}(x)$. This is compared to the average behavior of the homogeneous fault O1 (black). The average slip, slip rate and shear stress are given in Figures 7(a), (b) and (c), respectively. We observed an increase in complexity from homogeneity with these models; both O10 (red) and O15 (green) still experienced full system-wide rupture (large events that propagated over the full extent of the modeled fault). Full rupture nucleated from a smooth section of the fault and did not always arrest when compared to more localized ruptures that occurred in the O20, which had stronger barriers.

We see that, along with system-wide events, O10 (red) and O15 (green) also experienced small localized events that were arrested by neighbouring barriers. We defined these as "foreshock sequences" (discussed later in more detail) leading up to the mesoscopic main rupture (larger stress drop on system-wide events), highlighted in Figure 7(c). We see that as the order O is increased, the fault exhibits transition from well-behaved (homogeneous, O1) to visibly disordered system with full ruptures mixed with small localised ruptures (O10 and O15), then returning to well-behaved, creep-dominated faults with only small localized events on a preferential patch (O20).

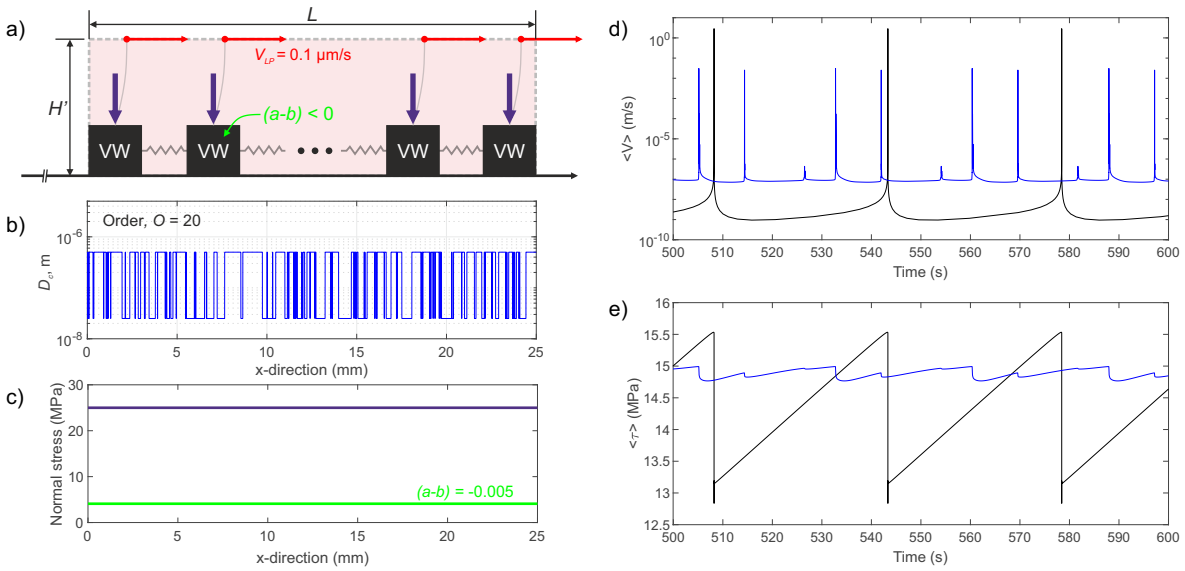

Figure 6. **(a)** General schematic showing the heterogeneous model. **(b)** Heterogeneous distribution of D_c, with O20. **(c)** Constant normal stress and VW rheology ($a - b < 0$) is shown along the x-axis. **(d)** Average slip velocity is given along the fault for the heterogeneous model (blue line), which is compared to the homogeneous model (black line). **(e)** Average shear stress along the fault for the heterogeneous model (blue line), which is compared to the homogeneous model (black line).

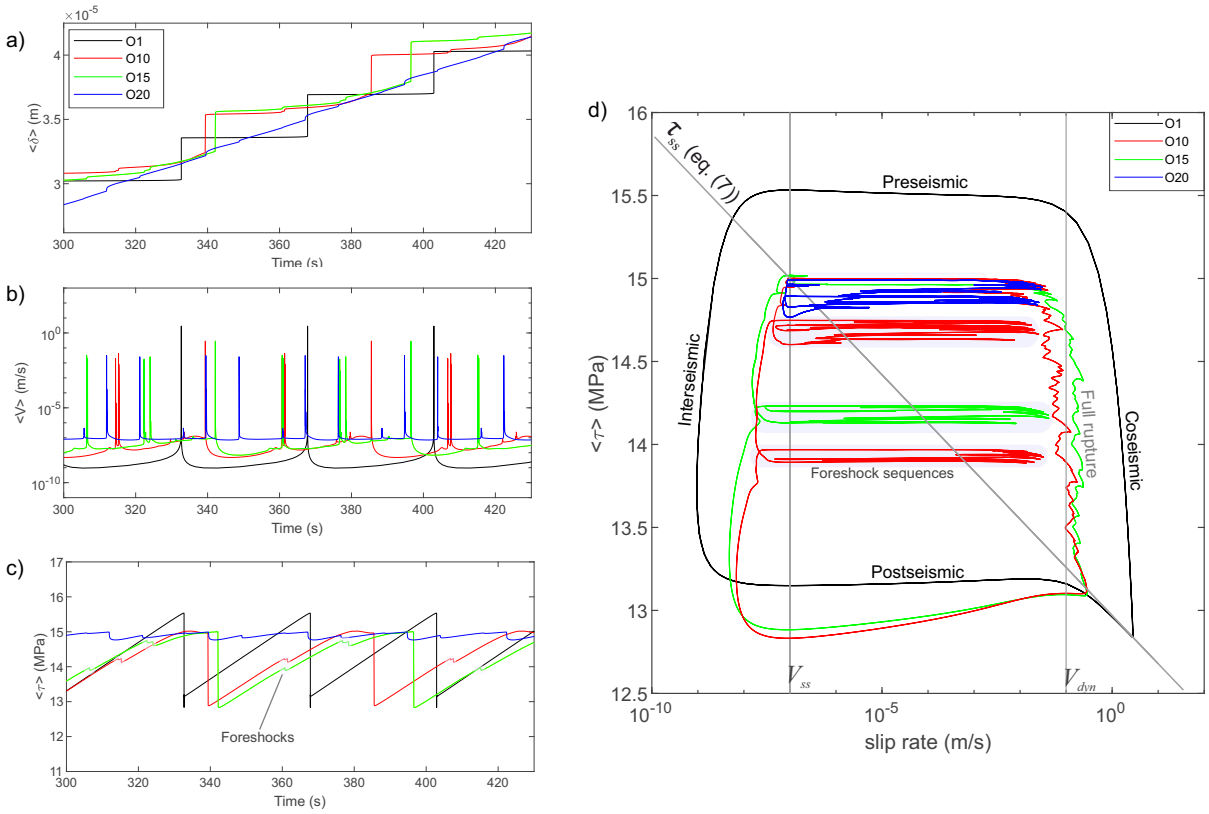

Figure 7. Three heterogeneous models $O = 10$ (red), 15 (green) and 20 (blue) are compared to the homogeneous model (black) for a short time window between 300 and 430 s. We show the **(a)** average slip, **(b)** average slip velocity and **(c)** average shear stress. We highlight where small drops in shear stress were seen and relate them to small localized events (foreshocks). **(d)** We examine the phase diagram between shear stress and slip velocity for each heterogeneous model compared to the homogeneous model.

To better visualize the system's behavior, we plot all models on phase-diagrams described in Figure 7(d) for all cases to compare to the homogeneous system response. The average cycles from co- to post- to inter- to pre-seismic behavior, moving around τ_{ss} in equation eq7. The O10 (red) and O15 (green) models appear to show, in general, lower total stress drops during full rupture events compared to the homogeneous case. We also see that during a full rupture, the average slip rate on these faults is generally lower than in the homogeneous case. For the most heterogeneous fault with the order O20, full rupture events did not occur but there was some deviation from steady state caused by small foreshock sequences that prevented the fault from simply 'creeping' along at a constant slip rate and steady state shear stress.

These foreshock sequences are highlighted in phase diagram (gray regions) (Figure 7(d)). Two major sequences were observed for the O10 and O15 models. The timing of these foreshock sequences, relative to the full fault cycle, are presented for O10(red) and occurred in the interseismic stages of the main rupture cycle. For O15(green), one foreshock sequence occurred in the interseismic portion and one occurred soon after the fault entered the nucleation phase of the larger rupture cycle. For O20 (blue), this smooth section of the fault prone to localized rupture behaved in a relative synchronous manner. More details to the spatio-temporal complexity of these ruptures are given in the next section.

3.2.1 Spatio-temporal behavior or precursory seismicity

In Figure 8 we examine the spatio-temporal evolution of the D_c-model with O17.5. This model was not presented in the previous section. The purpose of the previous section was to highlight changes in the general fault behavior at three levels of heterogeneity with distinctly different character. All spatio-temporal distributions of slip are depicted in a similar manner to Figure 8 in Supplemental Sections S3 for all models.

Figure 8(a) displays the spatio-temporal evolution of slip along the fault from time t = 300 s to 600 s. The time step between each isochron was uniform, taken every 30 intervals of adaptive time steps. We note that if any point on the fault slipped rapidly, the adaptive time step would decrease to accurately solve the boundary value problem. Seismicity (red slip isochrones) was defined as any node in the model experiencing slip velocities $V > V_{dyn}$ =0.177 m/s. Below this threshold the fault was assumed to slide

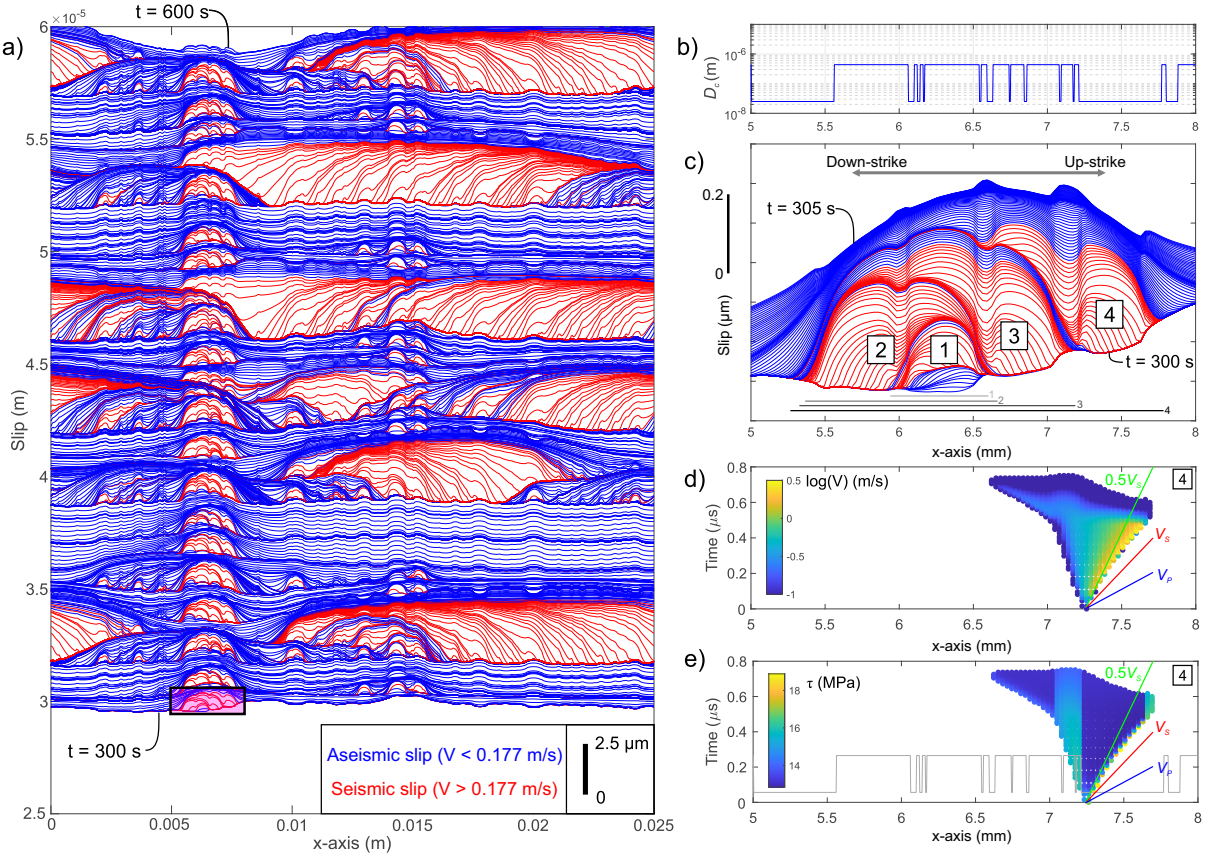

Figure 8. **(a)** Complex rupture for a fault with heterogeneity order $O = 17.5$. Slip along the fault are given for individual isochrones when the fault was sliding seismically (red, $V_{dyn} > 0.177$ m/s) or aseismically (blue, $V < 0.1$m/s). Results only present simulation times between $t = 300$ s and 600 s. We use these results to calculate the properties of the localized ruptures that showed local nucleation, dynamic rupture and arrest behavior due to heterogeneity in D_c. **(b)** Spatial heterogeneity for a dominant asperity of the fault from $x = 5$ to 8 mm. **(c)** A small sequence composed of four individual ruptures between time $t = 300$ s to 305 s on the dominant asperity. The rupture demonstrates complex distributions of slip and spatio-temporal distributions. To better understand the temporal changes of the rupture, we show the spatio-temporal evolution of Event 4 in terms of its **(d)** slip velocity and **(e)** shear stress.

aseismically (blue slip isochrones). Using this description we clearly identify certain 'seismic patches'.

One patch is highlighted in Figure 8(a) and enhanced in (c) where we examine slip on the transect $x = 5$ to 8 mm from $t = 300$ s to 305 s. This asperity section of the fault was prone to seismicity in all models, even the O20 that showed limited localized seismicity and we refer to this as *dominant asperity* from herein. Figure 8(b) demonstrates the spatial variability in heterogeneity in D_c along that section (for this case with O17.5). In Figure 8(c), we see that the fault slips aseismically between ruptures, which delineates the seismicity over these five seconds. Four individual ruptures are presented, which exhibited crack-like behavior but remain complex throughout the simulation due to the spatial variability in D_c, the level of heterogeneity (O17.5) and the continuously evolving shear stress on the fault.

In Figures 8(d) and (e) we investigate the space-time plot of slip velocity and shear stress, respectively, for Event 4 in the asperity failure sequence. The portion of the fault $x = 5$ to 8 mm is highlighted and we have superimposed the heterogeneity from Figure 8(b) for clarity. We see that Event 4 nucleates at the edge of a 'smooth-rough' boundary ($x \sim 7.25$ mm) depicted as the purple star. As the rupture expands, it propagates bi-laterally at different rates. We have superimposed three lines of constant velocity $0.5 \cdot V_S$ (green), V_S (red) and V_P (blue). Upon nucleation, the rupture propagates outward in a subsonic manner, moving faster ($\sim 0.75 \cdot V_S$) "up-strike" into the smoother, less resistive section than into the "down-strike", the rougher and more resistive section ($\sim 0.45 \cdot V_S$). This behavior represented typical rupture behavior for localized events on the dominant asperity.

The spatio-temporal rupture evolution for Event 4 is enlarged in Figure 9(d). Subsonic rupture propagation grows bi-laterally at different rates until arriving at separate barriers. Once the up-strike crack-tip (i.e. that moving on the smooth fault) reached an up-strike barrier, it was abruptly arrested (red star). As this rupture is arrested a back propagating front is emitted moving closer to the P wave velocity; this front is known as the P stopping phase. This stopping phase was observed by Madariaga (1976) in numerical simulations of kinematic rupture on a circular asperity. In that problem, the P stopping phase is the wave radiated when the rupture front suddenly haults (red stars), for example when it encounters a strong enough barrier. Both the up- and down-strike rupture encountered barriers and produced separate P stopping phases. For the down-strike propagating crack-

tip, this P stopping phase actually caused the overall dimension of the rupture to grow larger, eventually terminating at the green star.

To estimate the properties of each rupture we used an image detection algorithm (Gonzalez et al., 2009) and examined the 2-D distance-time space. Using the slip velocity threshold of $V_{dyn} > 0.177$ m/s, the ruptures were easily separated and the half-length L_r is displayed in Figures 9(d).

3.2.2 Constitutive behavior of individual ruptures

One goal of this study is to characterize, compare and validate our RSF model using source properties to those reported by Selvadurai (2019). We developed tools to quantify the cumulative slip (δ), static stress drop ($\Delta\sigma$), fracture energy ($G^{'}$) and rupture half-length (L_r) for each rupture to account for their individual complex behavior. In Figure 9 we look at the complex behavior of Event 4 from the previous section. Figure 9(d) reveals an enlarged view of Event 4 that ruptured a section with 1-D rupture dimension $2L_r$. To better understand the complex behavior of all seismic ruptures moving forward, we divide the full length of the rupture into 25 equally-spaced points along the x-axis. The number of transects used was sufficient to sample ruptures and to conduct a sensitivity study that investigated the number of required sampling transects (Supplementary Section S2).

Figure 9 provides a concise temporal understanding of the diversity in the temporal evolution of: (a) slip, (b) slip-rate and (c) shear stress along the spatial transects of Event 4. In Figure 9(a) the rupture has a non-uniform distribution of accumulated slip. The average slip along the 25 estimates was $\delta = 0.37$ μm. We use this to estimate the scalar seismic moment M_0 given by Aki (1966):

$$M_0 = GA\delta, \tag{13}$$

where A is fault area and δ is slip. For a penny-shaped fault $A = \pi r^2$ and for a square fault $A = (2L_r)^2$. Using this estimate the scalar seismic moment $M_0 = 0.0014$ N·m. This is equivalent to a moment magnitude $M_w = -7.94$. Transects were color coded for the smooth (red) and rough (black) sections of the fault to highlight differences in dynamic response. As expected, rougher sections showed higher variability in cumulative slip along each transect since they were responsible for arresting the rupture.

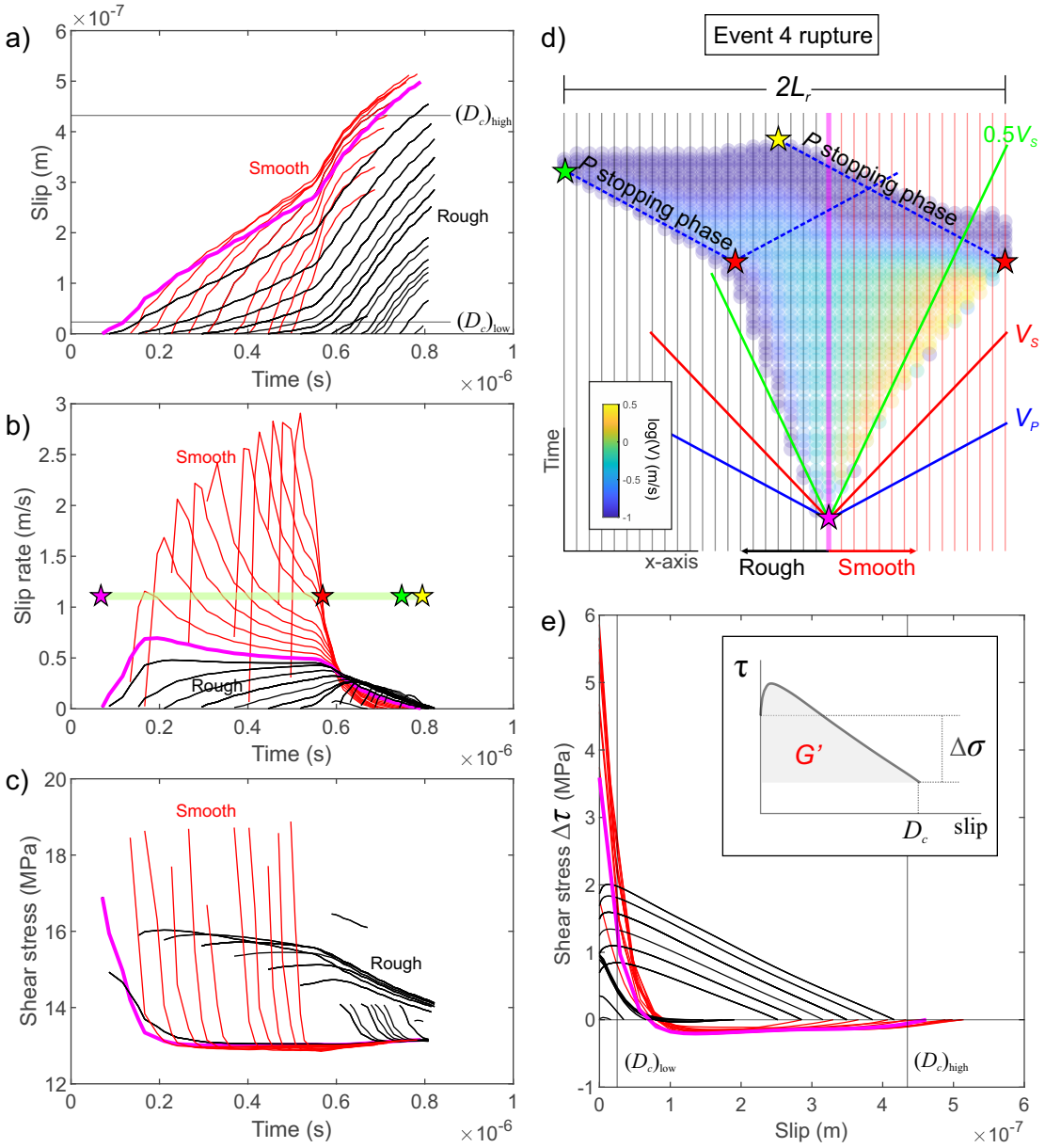

Figure 9. Rupture complexity of Event 4 in Figure 8(d) and (e) in space-time plots. **(a)** Temporal evolution of slip along 25 different transects of rupture spaced evenly on the fault. **(b)** Temporal evolution of slip rate along the transects in (a). Key instances of rupture are marked by the colored stars. **(c)** Temporal evolution of shear stress for the same positions as in (a). **(d)** Space-time plot of the rupture with the transects depicted graphically. **(e)** The traction-slip from each transect; the inset image depicts measurements of (static) stress drop ($\Delta\sigma$) and fracture energy ($G^{'}$) for each position on the fault.

The slip rate along each transect is displayed in Figure 9(b). For further clarity, important times of the rupture are marked by superimposed colored stars. The rupture has higher slip rates along the smoother section of the fault, whereas the rough section offers more resistance with lower slip rates. Shear stress along each transect is presented in Figure 9(c). Smooth portions of the fault (red lines) achieve higher peak stress and exhibit higher weakening rates than the rough sections (black lines), which offer higher resistance to rupture.

Figure 9(e) demonstrates the slip-traction relationship for each transect. Values are normalized with regards to the final stress. Using the inset image we can estimate the (static) stress drop ($\Delta\sigma$) and fracture energy ($G^{'}$). The latter is sometimes referred to as breakdown work defined by the area under the slip-traction curve (e.g., Tinti et al., 2005; Cocco et al., 2016). We find substantial differences in the participation of each surface (rough and smooth) in the metrics that have be extracted.

For clarity we have highlighted the critical slip weakening distance for both the smooth $D_{c,low}$ and rough section of the fault $D_{c,high}$. We see that in some cases slip was greater than $D_{c,high}$, which may be explained as dynamic overshoot (Madariaga, 1976). Calculating $\Delta\sigma$ is relatively straight forward; to determine the fracture energy $G^{'}$, we numerically integrated the area under this curve. For Event 4, the average static stress drop was $\Delta\sigma = 3.25$ MPa and average fracture energy $G^{'} = 0.13$ J/m^2.

3.3 Summary of precursory source properties

3.3.1 Seismic moment versus source size

In Figure 10(a) we examine the relationship between source area $A_r = (2 \cdot L_r)^2$ and seismic moment M_0 for the different RSF models. Source properties determined in the previous section are compared to those inferred from seismic waves from an in-depth study by Selvadurai (2019). We show the results five D_c-models (circles) against the kinematic estimates detailed by Selvadurai (2019) from P and S waves (triangles). Full ruptures referred to events that ruptured the entire fault surface. RSF ruptures followed the classical empirical scaling relationship between seismic moment and source geometry ($M_0 \propto L_r^3$). Figure 10(c) doisplays the relationship between stress drop and seismic moment, which was relatively constant $\sim$ 1.86 MPa where smaller ruptures had slightly lower values of stress drop.

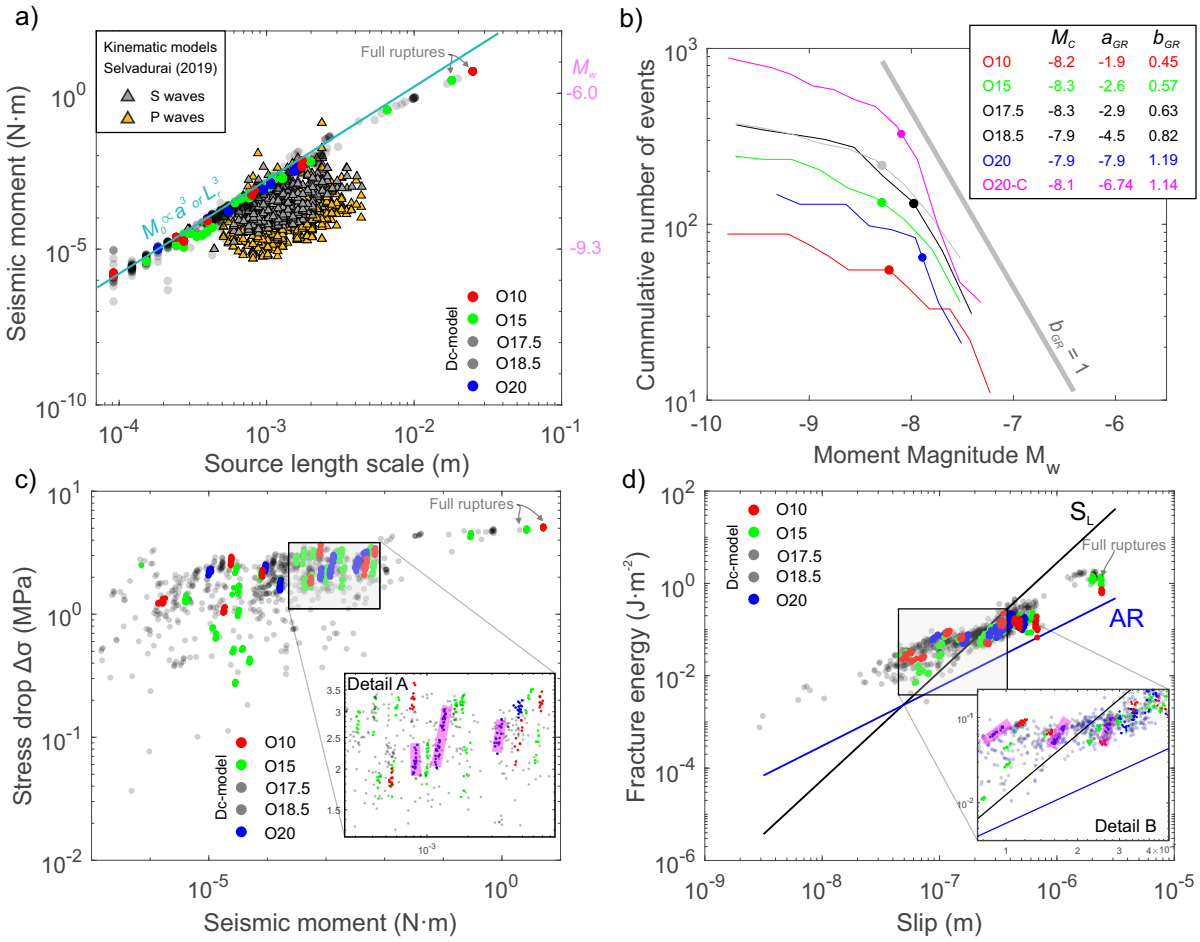

Figure 10. **(a)** Source length calculated from the numerical models with various levels of heterogeneity (colored circles) compared to their scalar seismic moment M_0. These are compared to the kinematic estimate of source properties determined using shear crack models Selvadurai (2019) for both P and S waves (triangles). **(b)** Frequency-magnitude distributions (FMDs) are given for each model catalog with $b_{GR} = 1$ depicted as reference. The inset legend gives the GR parameters: a_{GR}, b_{GR} and the magnitude of completeness M_c. **(c)** Relationship between stress drop ($\Delta\tau$) and ruptured area M_0. **(d)** Fracture energy (G') versus slip. We compare the models to empirical scaling estimates from laboratory seismicity (black line, Selvadurai, 2019) and extrapolated field estimates (blue line Abercrombie & Rice, 2005).

3.3.2 Frequency-magnitude distribution

Estimates of the frequency-magnitude distributions (FMDs) are shown in Figure 10(b). The Gutenberg-Richter (GR) law describes the magnitude distributions of earthquakes following the standard relationship $log_{10}(N) = a_{GR} - b_{GR}M_w$, where N is the number of events equal to or above magnitude M_w and a_{GR} and b_{GR} are constants describing the productivity and sizes of earthquakes, respectively (e.g. Wiemer & Wyss, 2002).

The legend gives the maximum likelihood estimate of the a_{GR}- and b_{GR}-values computed based on events above the magnitude of complete recording M_c (Wiemer & Wyss, 2002). Typically M_c is used to asses the completeness of the catalog under investigation, i.e. above which magnitude does the GR law fits the data best. We note that the nature of the GR relationship is scale-invariant and in our model, where all events can be recorded without converge bias, the completeness magnitude M_c is related to physical effect discussed later in Section 4.6. As the order of heterogeneity increases so do estimates of a_{GR}- and b_{GR}-values. Lower b_{GR} were observed on stick-slip dominant fault (O10 and O15) and increased on creeping faults (O20) which is discussed more thoroughly in Section 4.6.

3.3.3 Fracture energy scaling

Scaling behavior between fracture energy $G^{'}$ and slip δ is compared to the empirical relationship $G^{'} \propto \delta^{\gamma}$. In Figure 10(d) estimates of $G^{'}$ for the different models are presented. These are compared to the previously discussed empirical relationship for shear crack source models from laboratory experiments (S_L, γ =2.35) (Selvadurai, 2019) and estimates made at regional scales from natural earthquakes (AR, γ =1.28) following the observations of Abercrombie and Rice (2005) (see also Mai et al., 2006). We see that the results from the model tend to follow the same slope as AR but, if we look more closely, at Detail B in Figure 10(d), we see that some of the smooth patches show steeper trends in scaling. This can be explained by the fact that the preferential worn patches remain relatively constant in size but the stress drop varies, as depicted in Detail A of Figure 10(c).

3.3.4 Creeping to stick-slip transition

Figure 11 marks the average slip (black) and average shear stress (red) for 100 s of the simulations for strong barriers O20 (left-hand side, LHS) to weaker barriers O10 (right-hand side, RHS) and the transitional case O17.5 (middle panel). The general behavior of the fault

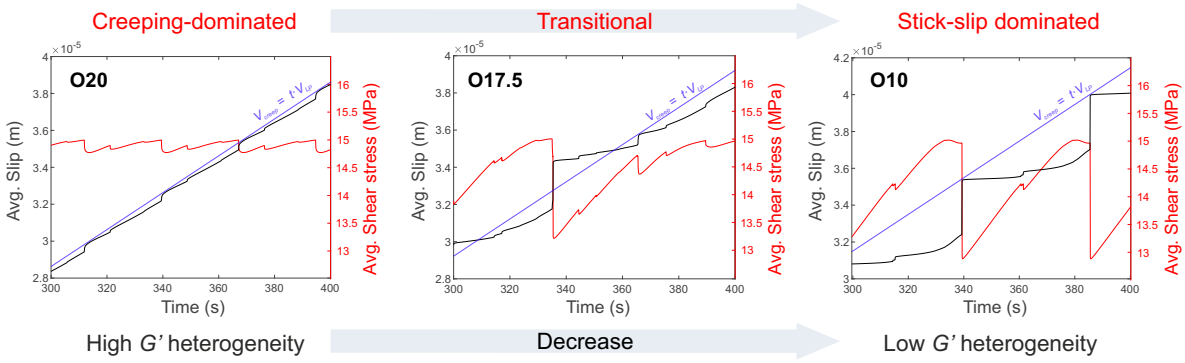

Figure 11. Earthquake recurrence rate for each D_c-model from higher O20 to lower O10 levels of strength heterogeneity. (**a**) The average behavior of the entire fault for small portions of time t =300 to 400 s for the O20 (creeping-dominated), O17.5 (transitional) and O10 (stick-slip dominated) models.

transitioned from creep-dominated (O20) to stick-slip dominated (O10). Creep-dominated and stick-slip dominated are defined by how much the average slip deviates from the creep rate ($V_{creep} = t \cdot V_{LP}$). This transition from creep- to stick-slip-dominant behavior occurred as the level of heterogeneity was decreased. In all simulations, the fault was driven at a constant loading rate and its impact on the general behavior is the subject of future work. Figure 11 highlights the distinct regimes and the appearance of foreshocks in a broad sense (Mogi, 1963, 1985) are discussed in Sections 4.1 and 4.2.

3.4 Heterogeneous *Composite*-model

The primary goal of this study is to provide an understanding of what types of RSF heterogeneity may explain a suite of experimental observations. Prior models have employed heterogeneity with a minimal level of unknown variables. We increase the complexity of the model using a Composite-model; this model aims to illuminate any additional complexity that may exist in the spatial distribution of normal stress. This model is presented to expand the possible boundary conditions that can feasibly explain the concomitant slow and fast slip on a frictional interface.

We use measurements from the pressure sensitive film (Figure 4(b)) to implement variability in normal stress. More information on the pressure sensitive film is given in Selvadurai and Glaser (2017). We use the scaling function where on smooth sections (low D_c) we prescribe constant normal stress $\sigma_{n,high} = 25$ MPa and on rough sections, we apply a constant

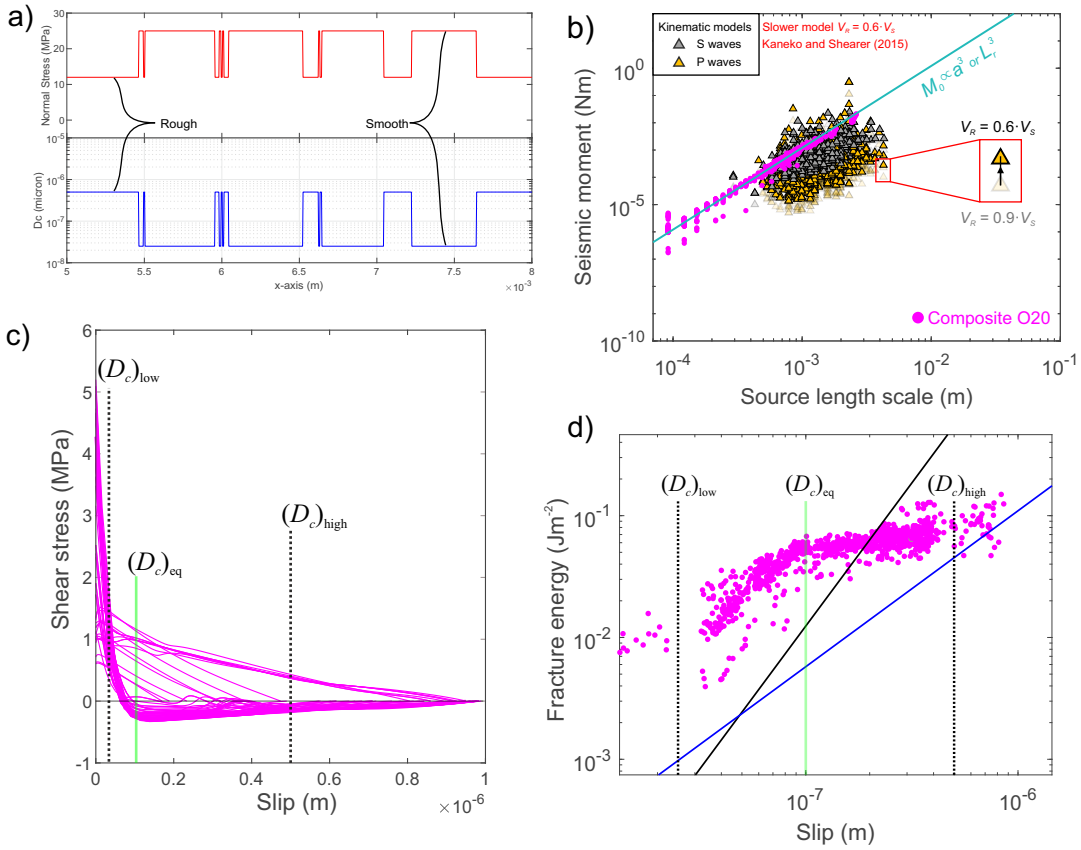

Figure 12. Results from the *Composite*-model. **(a)** A small section of the 1D fault from $x = 5$ to 8 mm showing the spatial variation in both D_c and σ_n. **(b)** The scaling relationship between A_r and M_0 (gray circles) is compared to the corrected kinematic estimates of source properties from Selvadurai (2019) (triangles). **(c)** Constitutive behavior for a large event in the *Composite*-model. **(d)** Relationship between fracture energy G' and slip δ. Empirical relationship between black and blue lines is similar to that demonstrated in Figure 10(d).

low normal stress level, set to the lower measurable limit of the pressure sensitive film $\sigma_{n,low}$ = 12 MPa (Selvadurai & Glaser, 2015b).

Figure 12(a) depicts a section of the spatial heterogeneity on the dominant asperity under normal stress σ_n (red) and at a critical slip weakening distance D_c (blue). The scaling function was chosen to be O20, a model that previously had a relatively well-behaved response. We use the same methods to calculate source properties and examine similar relationships for this composite-model (O20C).

Figure 12(b) reveals the relationship between M_0 and A_r, with similar estimates as the kinematic shear crack model in Figure 10(a). However, here we have made additional assumptions in the shear crack model regarding rupture speed. We apply a correction factor to account for slower ruptures in kinematic models, for example $V_r = 0.6 \cdot V_S$. This analysis was performed by Kaneko and Shearer (2015) for a range of rupture scenarios: circular or elliptical and symmetric or asymmetric. They found that decreasing the rupture speed can produce deviations of up to 2.5 times higher in terms of stress drop depending on the model and the wave phase (P or S). Average RSF estimates of rupture velocities were much lower $0.6 \cdot V_S$. From Table 1 in Kaneko and Shearer (2015), we updated the estimates from Selvadurai (2019), which minimized the difference between the kinematic (triangles) and RSF (circles) estimates of source properties. Original kinematic estimates are scaled by those from an asymmetric circular asperity model with rupture velocity $0.6 \cdot V_S$ leading to an increase in seismic moment by 2.63 for P wave estimates and 2.74 for S waves estimates.

Figure 12(c) displays the constitutive shear stress versus slip behaviour for a large random asperity. For reference, we mark the levels of $D_{c,low}$, $D_{c,eq}$ and $D_{c,high}$. The term $D_{c,eq}$, or equivalent critical slip weakening distance, appears to be a representative critical slip weakening distance that always lies between the two D_c limits but will likely vary for each rupture as a function of the ratio of high to low resistance of the interface participating in rupture. Looking at the relationship between $G^{'}$ and slip, we see that it appears to have a "kink". This kink is observed at about the slip level of $D_{c,eq}$.

4 Discussion

We have summarized findings from a well-documented laboratory experiment (Selvadurai & Glaser, 2015a, 2017; Selvadurai, 2019) that displayed complex nucleation behavior: preparatory slow preslip accompanied by intermittent localized seismicity from the same sections of the frictional interface (see Figure 1). A RSF model was developed to examine the complex frictional behavior using the rate- and state-dependent constitutive framework. The model accounted for wear observed from *a posteriori* measurements of roughness on the slider block surface that was well characterized in terms of a bimodal Gaussian distribution of surface roughness (Figure 2(a)). Attributes of our worn interface show a distinct polished surface embedded in a rougher surface, a feature that may be similar to the polished fault mirrors (FMs) observed on natural outcrops (see Figures 2(e) and (f)).

A cutting plane method (Figure 3) was used to mathematically quantify the spatial variation between smooth and rough sections. Two sets of RSF properties were chosen based on the fact that smooth surfaces have lower critical slip weakening distance D_c than rougher sections and the level of heterogeneity was investigated. The models showed complex behaviour (Figure 7) that differed from the homogeneous case (Figure 5); this could explain the experimental observation of concomitant slow slip and localized seismicity. We developed algorithms to isolate ruptures (Figures 8 and 9). These allowed us to estimate a range of source properties, such as scalar seismic moment (M_0), rupture length scale (L_r), seismic slip (δ), stress drop ($\Delta\tau$), fracture energy (G') and frequency-magnitude distributions (FMD) of five different D_c-models and a composite-model (Figures 10, 11 and 12). These calculations were compared to independently estimated seismological source properties made from interpretation of the seismic waves (Selvadurai, 2019).

4.1 'Cascade-up' nucleation behavior

Our model exhibits a wide range of behaviors, ranging from periodic (O1) to increasingly disordered (O10 to O18.5) then returning to more ordered (O20) (see Figure 7). In Figure 5 we observe that homogeneous rupture is well-behaved, exhibiting periodic stick-slip events at constant recurrence time. In the model, we assume periodic boundary conditions. This implies that if a rupture is not arrested within the mesoscopic region and reaches the boundary it would theoretically continue grow and rupture the full macroscopic region – cascading-up and creating a system-wide stick-slip event that was observed experimentally (Figure 1(b)).

We link full-rupture events to cascade-up nucleation processes forming from the initiation of a stuck patch (Noda et al., 2013; Selvadurai & Glaser, 2017; McLaskey, 2019). This assumption is plausible when looking at the hypocenter of the full-fault rupture (i.e. system-wide stick-slip event) measured experimentally in Selvadurai and Glaser (2015a). These were consistently located in the region near the roughness measurement (magenta star in Fig. 7 and 8 in Selvadurai & Glaser, 2015a). Moreover, this model appears to have produced rate-dependent cascade-up nucleation where foreshocks are a byproduct of the slow nucleation process but also small seismic 'ignitions' can initiate the full-rupture as described by rate-dependent cascade-up model (Noda et al., 2013; McLaskey, 2019).

In Figure 11, the two types of end-member behaviors are highlighted: 'creep dominated' and 'stick-slip dominated'. Stick-slip dominated behavior is described as supporting localized foreshocks sequences but also small events would cascade-up and trigger full ruptures. The creep dominated events form the O20 model were localized but they never developed into full ruptures. The D_c-models O10 and O15 exhibited foreshock sequences that were followed by a cascade-up into full ruptures (Figure 5), whereas O20 showed constrained ruptures that did not cascade-up.

Both the O10 and O20 models had identical level of normal stress σ_n leading to similar levels of peak and residual shear stress levels but the variations in D_c imposed differences in the weakening rates and fracture energy on the rough sections of each model. Therefore the order of the model was directly related to the the level of heterogeneity in fracture energy for our models. We found that for relatively low levels of fracture energy heterogeneity faults displayed a stick-slip-dominant behavior (foreshocks that can potentially cascade-up) and, once the heterogeneity is large enough, a creep-dominant behavior is observed. Hierarchical heterogeneity in fracture energy has been proposed by others (Ide & Aochi, 2005; Aochi & Ide, 2014, 2017) and will be discussed later.

While we cannot confirm an exact wear mechanism that may produce flat sections or increase the level of heterogeneity between smooth and rough sections, one hypothesis is that certain sections of the fault are more prone to flattening (ironing) and others will develop particles of gouge. Flattening, or 'ironing', of asperities due to adhesive wear has recently been investigated using a material independent framework (Aghababaei et al., 2016). Physics-based numerical simulations found a critical length scale describing the deformation mechanisms of interacting asperities. At length scales below a critical value, asperities flatten inelastically, dependent on the size of the asperity junction, the work of adhesion of the bulk material, and the maximum elastic strain energy that can be stored at a contact. This explanation fits observations made by Siman-Tov et al. (2013) and others that studied fault mirror formation in the laboratory. Brown and Scholz (1986) found that flattened patches could form upon the closure the interface indicating significant plastic flow at the highest points on the surface, albeit at smaller length scales than mirror surfaces studied and produced in the laboratory (Fondriest et al., 2013; Siman-Tov et al., 2013; Tisato et al., 2012; Siman-Tov et al., 2015).

Candela and Brodsky (2016) proposed plastic yielding, or grooving length scale that is controlled by the specific aspect ratio of roughenss asperities on the fault. They hypothesised that the minimum grooving length scale is related to the critical slip weakening parameter D_c arguing that plastic yielding combined with scale-dependent roughness define the process that sets the scale of the relevant asperities. This argument is similar to our arguments and links variations in worn distribution of D_c presented here to seismicity on larger length scales in natural faults. While temperature, fluid and chemical processes observable on natural faults make the conjecture that simple laboratory experiments of solid friction have no bearing on real faults. Candela and Brodsky (2016) suggests the opposite and the preserved fingerprint on natural fault surfaces of the fundamental process governing solid friction.

4.2 Dominant asperity

All models hinged about the behavior of specific section of the fault from $x = 5$ mm to 8 mm, we referred to as the dominant asperity (Figure 8(b) and (c)). In all models, this section produced localized events. With lower levels of heterogeneity (O10 and O15), foreshocks were produced from this asperity that also possessed the potential of cascading runaway rupture. In Supplemental Sections S3, we show spatio-temporal evolution of slip of O10 and the O15 full-ruptures, in which breakdown occurs in a similar manner – nucleating each time from the dominant asperity. This dominant asperity behaved at times as an ignition site for the nucleation of gross fault rupture and this may be similar to behaviors of asperities predisposed to seismicity in nature.

This type of behavior may explain the observations in the Naka-Oki region in eastern Japan (Okuda & Ide, 2018a) and the Tohoku–Hokkaido subduction zone, Japan (Ide, 2019). Where earthquakes shared almost identical growth offering patterns for repeating events of various sizes. This observation appears to be consistent with our model, an explanation that repeater asperities that routinely produce $M_w \sim 2$ could have structures in that sometimes allow for it to cascade-up to $M_w \sim 4.8$ (Okuda & Ide, 2018b). These authors hypothesize that a hierarchical structure exists (as depicted in fig. 5 of Okuda & Ide, 2018a), possibly due to heterogeneity in the fracture energy (Ide & Aochi, 2005; Aochi & Ide, 2014, 2017). Our model agrees with this hypothesis and heterogeneity in fracture energy is provided in the form of polished smooth sections in a rougher interface that does not exhibit large out of plane roughness-induced barriers.

We also observe interesting behavior surrounding the unlocking sequence of the dominant asperity in Figure 8(c). For clarity, the temporal unlocking sequence for the O17.5 model were enumerated in ascending order from 1 to 4. Below the spatio-temporal slip evolution (red and blue isochrons), we show the spatial length of each rupture. We can see that each rupture overlaps the previous rupture, a phenomenon was also observed by Okuda and Ide (2018b) and referred to as 'streaking', which they claimed explained the patches of differing sizes possessing some hierarchical structure. This also might be similar to the dynamic precursor detachment fronts observed experimentally on fault analogs (Rubinstein et al., 2004, 2006) and the breakdown fronts seen on granite-granite interfaces by (Ke et al., 2018). Okuda and Ide (2018b) attribute this specific rupture process to subtle differences in the physical conditions of the fault interface, which appear to be consistent with a fault interface consisting of a series of hierarchical structures. Our model produced foreshocks in a broad sense (Mogi, 1985) and was due to the patchy distribution of fracture energy on our smooth/rough frictional fault idealization.

Mogi (1963) inferred the crustal structure in Japan from the records of seismic gaps, swarms, aftershocks and foreshocks (see also Mogi, 1985). He found that regions with less fracturing appear to correlate to the newer observations of repeating streakers and the cascade-up style seismic signatures discussed here (Okuda & Ide, 2018a, 2018b; Ide, 2019). As noted by Wang and Bilek (2014), there are positive correlation between large events and smooth subducting segments of seafloor that may become increasingly smoothed (over millions of years) by wearing of the interface with the large amount of sediments. While more study is required, producing frictional models with proper stochastic distribution of frictional properties that are able to reproduce the complex observational behavior (streaking repeaters capable of cascade-up style-behavior) should be a point of discussion in the future (see further discussion in Section 4.7).

4.3 Repeating-like behavior

In contrast to the cascade-up behavior discussed above, the dominant asperity ($x =$ 5 mm to 8 mm) also showed quite regular behavior when the level of heterogeneity was increased to O20. Spatio-temporal evolution of slip from 300 s to 600 s for the O20 model is also given in Supplemental Section S3. For this model, the average shear stress and slip rates remained near steady state (equation eq7) and the only deviation came from the local increase in slip rate during ruptures of the dominant asperity. In Figure 11 we refer

to this as 'creep-dominated'. For our creep-dominated fault, any event produced by the dominant asperity was easily arrested by the rougher surroundings, which in the model, were actually regions exhibiting relatively larger fracture energy. This 'creep-dominated' behavior is similar to that observed for repeating earthquakes in nature (e.g., Beeler et al., 2001; Uchida, 2019)

Models used to understand repeating earthquakes typically involve a circular asperity embedded on a planar fault, where the asperity is relatively locked with respect to the creeping region that loads a resistive asperity. When studied using RSF laws, the creeping region is typically given velocity-strengthening (VS, $(a-b)>0$) properties and the asperity is velocity-weakening (VW, $(a-b)<0$) (N. Kato, 2003; Chen & Lapusta, 2009). In our models, seismicity only occurs on the VW asperity and their ability to trigger more complex behavior, e.g. a cascade-up style rupture, cannot exist unless additional heterogeneity to VW regions are specified. Noda et al. (2013) looked at the behavior of smaller VW asperities embedded on a larger VW asperity while varying ratios of RSF properties and found complex model behavior. Our model finds that, due to the heterogeneity the in polished-to-rough surface, we can actually host constrained repeating earthquakes in an entirely VW region that depends on the level of heterogeneity. As heterogeneity increases between the polished and rough sections, repeating events and creep-dominated behavior may become more apparent.

4.4 Nucleation/arrest of crack-like ruptures

Figures 8(d) and (e) summarized the behavior of a crack-like rupture typically seen on the dominant asperity. Nucleation of the precursory events mostly occurred on the boundaries between the smooth-rough transition on the VW interface. This type of behavior has been observed in a larger scale 2D RSF simulation of the Parkfield section of the San Andreas Fault, CA, USA (Barbot et al., 2012), in conceptual models of interacting asperities (N. Kato, 2003) and complex megathrust subduction zones (Kaneko et al., 2010); however, nucleation in these models occur frequently at a VS-VW transition.

From Figure 9, we see that the smoother ruptures were more efficient, reaching higher slip rates, having higher stress drop and producing less fracture energy. Slower rupture speeds coupled with less stress drop and higher fracture energies occurred on sections that had a "rough" parameterization, which was as expected. The complex interaction of how the rupture that propagated on both a polished and rough interface was apparent even as

it decelerated, when the P waves stopping phase was observed (Madariaga, 1976). This stopping phase appears to be reflected or emanating from the smooth-rough boundaries.

4.5 Dynamic RSF source properties

The model displays great complexity at the mesoscopic (Figure 7) and microscopic scales (Figures 8 and 9). Dynamic RSF source estimates of moment to source length scale followed the standard $M_0 \propto L_r^3$, which also matched kinematic estimates in Selvadurai (2019). While the dynamic and kinematic source estimates highlighted here differ slightly, the magnitude and trends between estimates are similar even though the problem is approached from two different modeling frameworks. Comparing these two different models is an important step towards validating the effectiveness of each model and understanding how to link precursory seismicity to the nucleation phase on fault analogs. Identical validation efforts have been used for RSF models looking at repeating earthquakes in Parkfield, CA (Chen & Lapusta, 2009).

Stress drop is dependent on the rupture velocity (V_r) (Kaneko & Shearer, 2015). We found our crack-like rupture to be much slower ($0.6 \cdot V_S$) than those typically used in kinematic approaches, where kinematic shear crack models assume rupture velocities between 0.9 and $1.0 \cdot V_S$ (Cocco et al., 2016; Selvadurai, 2019). With this additional knowledge, updates to our original kinematic estimates were made by applying correction factors from numerical studies performed by Kaneko and Shearer (2015). This correction factor increased the correlation between kinematic estimates and RSF estimates. Using more accurate estimates of rupture velocity when estimating source features via kinematic crack-models should be done carefully and investigated in more detail (e.g. McGuire & Kaneko, 2018).

Fracture energy $G^{'}$ versus slip was compared for two types of model (D_c and composite) with scaling relationships in the lab (S_L) and field (AR). The D_c model followed the AR scaling relationship more closely, which we attribute to the fact that ruptures occurred with the rougher (more resistive) portions more than in the composite model. Perhaps this was due to the description of heterogeneity in the models. The D_c-model had a constant shear strength and, therefore, heterogeneity in both the slip-weakening rate and fracture energy on the polished/rough sections controlled the source properties. The Composite-model added to the complexity by including normal stress variability, causing an additional heterogeneity in the shear strength of the fault (see equation eq5). This additional complexity caused

more localized seismicity that occurred because of larger contrasts in slip-weakening rate and less contrast in the fracture energy between the polished and rough sections. This is clearly seen in the O20 and O20-C spatio-temporal distributions of slip that shown in detail in Supplemental Figures S3.4 and S3.5, respectively. The composite model nucleated more events but, similar to the less complex model, there was no cascade-up rupture. In the composite model, geometrically smaller smooth sections could nucleate rupture but they would arrest due to the lower strength of the rough region. The purpose of this study was to provide a reasonable parameter space (Figure 4) based on a suite of experiments that, when combined with a novel RSF model, provides insight into the potential behaviors of worn faults in nature.

4.6 Effect of fracture energy heterogeneity on FMDs

Analysis of the FMDs showed that creeping faults (O20 and O20-c) had higher b_{GR}- and a_{GR}-values than stick-slip dominant faults (O-10 and O15). A gradual transition was observed from both low to high a_{GR}- and b_{GR}-values as the heterogeneity in fracture energy was increased. This observation follows studies in natural tectonic settings where creeping sections were found to have higher b-values than locked section prone to larger earthquake (Amelung & King, 1997; Tormann et al., 2014). Goebel et al. (2013) found that temporal decreases in laboratory estimates of b-values occurred moments leading up to larger stick-slip events, a phenomena that has been observed in natural tectonic settings prior to large megathrust events (Tormann et al., 2015; Gulia et al., 2016; Gulia & Wiemer, 2019). Our model suggests that lower b-values may occur on faults that also experience foreshock behavior and both observations can be reconciled by a hierarchical structure of the fault that exhibits low (but distinct) variations in fracture energy distribution, which is a point of study moving forward.

Completeness in our model is associated with the minimum size of resolvable earthquake defined by the mesh scheme and solution convergence (Supplemental Section S1). This differs from the field where M_c is affected by the fact that the recording network is only capable of recording a fraction of all events for magnitudes smaller (Wiemer & Wyss, 2002). By definition, the Gutenberg-Richter law is scale-invariant above the magnitude of the completeness threshold (M_c). Below this threshold, the size and occurrence of seismicity is scale-variant. From a statistical perspective, events falling below M_c are not used and using more involved methods that investigate the catalog behavior near and below M_c will

be useful (Mignan, 2012, 2020). While scale invariance is produced by our model, a large number of events fall below this threshold and are likely due to the scale-variant mechanism associated with the smoothing of high asperities during the wearing process. More extensive studies will be needed but we note scale variant features, such as the dominant asperity, had important impact on critical aspects of nucleation physics, such as the generation of foreshocks and cascade-up style failure, which may be useful for earthquake forescasting and prediction.

Understanding whether regions susceptible to foreshocks and rate-dependent cascade-up style failure would impose a break in the empirically observed scaling of seismicity (Scholz, 1997) or if they simply correspond to the statistical superposition of power law brittle-failure type process and a point repeater-like process at a characteristic length scale, could help us understand how these potentially important hierarchical structures affect our ability to interpret statistical tools for hazard and risk in these regions.

4.7 RSF properties on worn sections of faults

In Section 1.3, we highlighted findings from tribology in which wearing of surfaces can produce nanometrically smooth regions in an overriding rougher surface that is well-characterized by the bi-modal Gaussian PDF of surface height. These polished sections have also been linked to fault mirrors through laboratory tests under a range of conditions (slow and fast sliding and at high-temperature). Laboratory experiments give explanations as to why these FMs exist on exposed outcrops but do not give the extent of how large they may grow due to constraints of typical laboratory studies that produce them. Unfortunately, our understanding of polished fault mirrors from exposed outcrops is constrained by our ability to observe them; an obvious limitation exists when we compared the volume of exposed outcrops to the volume of active faults producing seismicity in nature.

Our model suggests that the scale of polished sections to rough sections is important; correspondingly, we conjecture that attempting to capture this using the single fractal measurement of the Hurst exponent is not adequate (the scale at which needs more investigation). Since the mirrors in our model required a bi-modal Gaussian distribution of surface heights, new research into fractal characterization of such surfaces by Hu et al. (2019a) suggests that a bi-fractal distribution in roughness is more representative (Leefe et al., 1998; Pawlus, 2008). These surfaces have already been shown to influence characteristics of acous-

tic emission energy release upon sliding (Fan et al., 2010; Hu et al., 2019b) but these results are recent and more investigation is required. Bi-modal Gaussian and b–fractal stochastic descriptions of frictional parameters may help us understand complex frictional behavior, such as faults where rate-dependent cascade-up physics have been observed.

5 Conclusions

We developed RSF to capture slow aseismic transients coupled with localized foreshocks and compared this to similar behavior observed in a concerted laboratory experiment on a fault analog. Heterogeneity was necessary and prescribed using the worn surface roughness that displayed a bimodal Gaussian distribution of surface heights. We discretized smooth and rough faults using an understanding the micro-mechanics of the critical slip D_c where smooth sections have lower values. This resulted in polished sections (mirrors) producing small ruptures, whereas rougher sections hosted aseismic slip.

The behavior of the fault varied between creep-like to stick-slip dominated and depended on the level of heterogeneity in the fracture energy. Small localized events were particularly interesting around a dominant asperity that produced seismicity in every simulation and appeared to control cascade-up-breakdown of the fault when the level of fracture energy heterogeneity was low.

Seismic source properties were validated against independent kinematic estimates from elastodynamic ground motions. Rupture velocity obtained from the RSF models estimated that subsonic ruptures propagated at speeds close to $V_r = 0.6 \cdot V_S$. This was used to adjust kinematic source properties by Selvadurai (2019) for the slower crack-like ruptures. Validating the RSF source properties was deemed sufficient for a first-order understanding of the modeled frictional heterogeneity that may explain simultaneous foreshocks and aseismic preslip. We believe that this should be further explored in more robust parametric studies.

Worn faults observed in nature have the form of fault mirrors but it is unclear how they truly evolve over geologic time, their spatial extent and how this evolution affects the frictional response of a shear principal slip zone. In our wear-based model, changes in the level of heterogeneity in fracture energy caused end-member behavior from creep to stick-slip dominant. Future experiments will need to investigate this behavioral evolution and potentially update the stochastic descriptions of frictional parameters on faults that contain FMs.

Acknowledgments

We would like to thank T. Yamaguchi, L. Villiger, B. Edwards T. Tormann, P. Bhattacharya and A. Mignan who provided important discussion points regarding the analysis. Key insights into simulations presented here are given by J.-P. Ampuero. This research was supported by: JSPS KAKENHI Grant Number JP16H06478 in Scientific Research on Innovative Areas "Science of Slow Earthquakes". Computational resources were provided by the Information Technology Division and Extreme Computing Research Center (ECRC) at KAUST. Funding for parts of this research was provided by the National Science Foundation Grant CMMI-1131582 awarded to SDG at the University of California, Berkeley. Funding for PAS was provided through the OFES Project: EDGAR - Dimensionnement du réseau de fractures dans les réservoirs géothermaux (Contract SI/501495-01). PMM's contribution to this study and a research visit of PAS to KAUST was supported by KAUST research grant BAS/1/1339-01-01. Finally, the authors assume full responsibility for the comments and concepts presented in the paper.

All data sets required to reproduce the results presented here are freely available at this site (doi.org/10.3929/ethz-b-000405620). Please contact the corresponding author for access.

References

Abercrombie, R. E., & Rice, J. R. (2005). Can observations of earthquake scaling constrain slip weakening? *Geophysical Journal International*, *162*(2), 406–424. Retrieved from `http://dx.doi.org/10.1111/j.1365-246X.2005.02579.x` doi: 10.1111/j.1365-246X.2005.02579.x

Adachi, K., & Kato, K. (2000). Formation of smooth wear surfaces on alumina ceramics by embedding and tribo-sintering of fine wear particles. *Wear*, *245*(1), 84–91. Retrieved from `http://www.sciencedirect.com/science/article/pii/S0043164800004683` doi: http://dx.doi.org/10.1016/S0043-1648(00)00468-3

Aghababaei, R., Warner, D. H., & Molinari, J. F. (2016). Critical length scale controls adhesive wear mechanisms. *Nature Communications*, *7*(11816).

Aki, K. (1966). Generation and propagation of G waves from the Niigata Earthquake of June 16, 1964. Part 2. Estimation of earthquake movement, released energy, and stress-strain drop from the G wave spectrum. *Bull. Earthq. Res. Inst.*, *44*, 73–88. Retrieved from `https://ci.nii.ac.jp/naid/10006221613/en/`

Amelung, F., & King, G. (1997, September). Earthquake scaling laws for creeping and non-creeping faults. *Geophysical Research Letters*, *24*(5), 507–510. Retrieved from https://doi.org/10.1029/97GL00287 doi: 10.1029/97gl00287

Ampuero, J. P., & Rubin, A. M. (2008). Earthquake nucleation on rate and state faults: Aging and slip laws. *Journal of Geophysical Research*, *113*, B01302. doi: 10.1029/2007JB005082

Aochi, H., & Ide, S. (2014). Ground motions characterized by a multi-scale heterogeneous earthquake model. *Earth, Planets and Space*, *66*(42).

Aochi, H., & Ide, S. (2017, July). Role of multiscale heterogeneity in fault slip from quasi-static numerical simulations. *Earth, Planets and Space*, *69*(1), 94. Retrieved from https://doi.org/10.1186/s40623-017-0676-5

Barbot, S., Lapusta, N., & Avouac, J. (2012). Under the Hood of the Earthquake Machine: Toward Predictive Modeling of the Seismic Cycle. *Science*, *336*(6082), 707-710. Retrieved from http://www.sciencemag.org/content/336/6082/707.abstract doi: 10.1126/science.1218796

Beeler, N. M., Lockner, D. L., & Hickman, S. H. (2001, 12). A Simple Stick-Slip and Creep-Slip Model for Repeating Earthquakes and its Implication for Microearthquakes at Parkfield. *Bulletin of the Seismological Society of America*, *91*(6), 1797–1804. Retrieved from https://doi.org/10.1785/0120000096 doi: 10.1785/0120000096

Ben-David, O., Cohen, G., & Fineberg, J. (2010). The Dynamics of the Onset of Frictional Slip. *Science*, *330*(6001), 211–214. doi: 10.1126/science.1194777

Ben-Zion, Y. (2008, August). Collective behavior of earthquakes and faults: Continuum-discrete transitions, progressive evolutionary changes, and different dynamic regimes. *Reviews in Geophysics*, *46*(4). Retrieved from https://doi.org/10.1029/2008RG000260 doi: 10.1029/2008rg000260

Beroza, G. C., & Ellsworth, W. L. (1996). Properties of the seismic nucleation phase. *Tectonophysics*, *261*(1-3), 209–227. doi: http://dx.doi.org/10.1016/0040-1951(96)00067-4

Berthoude, P., Baumberger, T., G'Sell, C., & Hiver, J. M. (1999). Physical analysis of the state- and rate-dependent friction law: Static friction. *Physical Review B: Condensed Matter and Materials Physics*, *59*(22), 14313–14327. doi: 10.1103/PhysRevB.59.14313

Bhattacharya, P., Rubin, A. M., Bayart, E., Savage, H. M., & Marone, C. (2015). Critical

evaluation of state evolution laws in rate and state friction: Fitting large velocity steps in simulated fault gouge with time-, slip-, and stress-dependent constitutive laws. *Journal of Geophysical Research: Solid Earth*, *120*(9), 6365–6385. doi: 10.1002/2015JB012437

Borucki, L. (2002). Mathematical modeling of polish-rate decay in chemical-mechanical polishing. *Journal of Engineering Mathematics*, *43*(2), 105–114. Retrieved from http://dx.doi.org/10.1023/A:1020305108358 doi: 10.1023/A:1020305108358

Borucki, L. J., Witelski, T., Please, C., Kramer, P. R., & Schwendeman, D. (2004). A theory of pad conditioning for chemical-mechanical polishing. *Journal of Engineering Mathematics*, *50*(1), 1–24. Retrieved from http://dx.doi.org/10.1023/B:ENGI.0000042116.09084.00 doi: 10.1023/B:ENGI.0000042116.09084.00

Bouchon, M., Durand, V., Marsan, D., Karabulut, H., & Schmittbuhl, J. (2013, April). The long precursory phase of most large interplate earthquakes. *Nature Geoscience*, *6*(4), 299-302. Retrieved from http://dx.doi.org/10.1038/ngeo1770

Bouchon, M., Karabulut, H., Aktar, M., Ozalaybey, S., Schmittbuhl, J., & Bouin, M. P. (2011). Extended nucleation of the 1999 M_w 7.6 Izmit earthquake. *Science*, *331*(6019), 877-880. doi: 10.1126/science.1197341

Bouissou, S., Petit, J. P., & Barquins, M. (1998, February). Normal load, slip rate and roughness influence on the polymethylmethacrylate dynamics of sliding 1. Stable sliding to stick-slip transition. *Wear*, *214*(2), 156–164. Retrieved from http://www.sciencedirect.com/science/article/pii/S0043164897002421

Brodsky, E. E., Gilchrist, J. J., Sagy, A., & Collettini, C. (2011). Faults smooth gradually as a function of slip. *Earth and Planetary Science Letters*, *302*, 185–193. Retrieved from http://www.sciencedirect.com/science/article/pii/S0012821X10007624 doi: doi.org/10.1016/j.epsl.2010.12.010

Brodsky, E. E., Kirkpatrick, J. D., & Candela, T. (2016). Constraints from fault roughness on the scale-dependent strength of rocks. *Geology*, *44*(1), 19–22.

Brodsky, E. E., & Lay, T. (2014). Recognizing Foreshocks from the 1 April 2014 Chile Earthquake. *Science*, *344*(6185), 700–702. doi: 10.1126/science.1255202

Brown, S. R., & Scholz, C. H. (1986, September). closure of rock joints. *Journal of Geophysical Research Solid Earth*, *91*(B5), 4939–4948. Retrieved from https://doi.org/10.1029/JB091iB05p04939 doi: 10.1029/jb091ib05p04939

Buijze, L., Guo, Y., Niemeijer, A. R., Ma, S., & Spiers, C. J. (2020). Nucleation of stick-slip

instability within a large-scale experimental fault: Effects of stress heterogeneities due to loading and gouge-layer compaction. *Journal of Geophysical Research: Solid Earth*, *n/a*(n/a), e2019JB018429. Retrieved from https://agupubs.onlinelibrary.wiley.com/doi/abs/10.1029/2019JB018429 doi: 10.1029/2019JB018429

Bürgmann, R. (2004). Warning signs of the Iquique earthquake. *Nature*, *512*, 258–259.

Bürgmann, R., Schmidt, D., Nadeau, R. M., d'Alessio, M., Fielding, E., Manaker, E., ... Murray, M. H. (2000). Earthquake Potential Along the Northern Hayward Fault, California. *Science*, *289*, 1178-1182.

Candela, T., & Brodsky, E. E. (2016). The minimum scale of grooving on faults. *Geology*, *44*(8), 603–606.

Candela, T., Renard, F., Bouchon, M., Marsan, D., Schmittbuhl, J., & Voisin, C. (2009). Characterization of Fault Roughness at Various Scales: Implications of Three-Dimensional High Resolution Topography Measurements. *Pure and Applied Geophysics*, *166*, 1817–1851. doi: 10.1007/s00024-009-0521-2

Chen, T., & Lapusta, N. (2009). Scaling of small repeating earthquakes explained by interaction of seismic and aseismic slip in a rate and state fault model. *Journal of Geophysical Research: Solid Earth*, *114*(B1). Retrieved from https://agupubs.onlinelibrary.wiley.com/doi/abs/10.1029/2008JB005749 doi: 10.1029/2008JB005749

Ciavarella, M. (2016). On the effect of wear on asperity height distributions, and the corresponding effect in the mechanical response. *Tribology International*, *101*, 164–167. Retrieved from http://www.sciencedirect.com/science/article/pii/S0301679X16300858 doi: http://doi.org/10.1016/j.triboint.2016.04.031

Cocco, M., Tinti, E., & Cirella, A. (2016). On the scale dependence of earthquake stress drop. *Journal of Seismology*, *20*, 1151–1170. doi: https://doi.org/10.1007/s10950-016-9594-4

Dieterich, J. H. (1978). Preseismic fault slip and earthquake prediction. *Journal of Geophysical Research*, *83*(B8), 3940–3948. doi: 10.1029/JB083iB08p03940

Dieterich, J. H. (1979). Modeling of rock friction: 1. Experimental results and constitutive equations. *Journal of Geophysical Research*, *84*(B5), 2161–2168. doi: 10.1029/JB084iB05p02161

Dieterich, J. H. (1992). Earthquake nucleation on faults with rate-and state-dependent strength. *Tectonophysics*, *211*(1), 115–134. Retrieved from http://www.sciencedirect.com/science/article/pii/004019519290055B doi: https://

doi.org/10.1016/0040-1951(92)90055-B

Dodge, D. A., Beroza, G. C., & Ellsworth, W. L. (1995). Foreshock sequence of the 1992 Landers, California, earthquake and its implications for earthquake nucleation. *Journal of Geophysical Research*, *100*(B6), 9865–9880. doi: 10.1029/95JB00871

Dodge, D. A., Beroza, G. C., & Ellsworth, W. L. (1996). Detailed observations of California foreshock sequences: Implications for the earthquake initiation process. *Journal of Geophysical Research*, *101*(B10), 22371–22392. doi: 10.1029/96JB02269

Dreger, D., Nadeau, R. M., & Chung, A. (2007). Repeating earthquake finite source models: Strong asperities revealed on the San Andreas fault. *Journal of Geophysical Research*, *34*, L23302. doi: 10.1029/2007GL031353

Dunham, E. M., Belanger, D., Cong, L., & Kozdon, J. E. (2011). Earthquake Ruptures with Strongly Rate-Weakening Friction and Off-Fault Plasticity, Part 2: Nonplanar Faults. *Bulletin of the Seismological Society of America*, *101*(5), 2308. Retrieved from `http://dx.doi.org/10.1785/0120100076` doi: 10.1785/0120100076

Ellsworth, W. L., & Beroza, G. C. (1995). Seismic evidence for an earthquake nucleation phase. *Science*, *268*(5212), 851-855. doi: 10.1126/science.268.5212.851

Fan, Y., Gu, F., & Ball, A. (2010, February). Modelling acoustic emissions generated by sliding friction. *Wear*, *268*(5), 811–815. Retrieved from `http://www.sciencedirect.com/science/article/pii/S0043164809006322`

Fang, Z., & Dunham, E. M. (2013). Additional shear resistance from fault roughness and stress levels on geometrically complex faults. *Journal of Geophysical Research: Solid Earth*, *118*(7), 3642–3654. doi: 10.1002/jgrb.50262

Fineberg, J., & Bouchbinder, E. (2015, November). Recent developments in dynamic fracture: some perspectives. *International Journal of Fracture*, *196*(1), 33–57. Retrieved from `https://doi.org/10.1007/s10704-015-0038-x`

Fondriest, M., Smith, S., Candela, T., Nielsen, S. B., Mair, K., & Di Toro, G. (2013, 11). Mirror-like faults and power dissipation during earthquakes. *Geology*, *41*(11), 1175-1178. Retrieved from `https://doi.org/10.1130/G34641.1` doi: 10.1130/G34641.1

Fukuyama, E., Tsuchida, K., Kawakata, H., Yamashita, F., Mizoguchi, K., & Xu, S. (2018). Spatiotemporal complexity of 2-D rupture nucleation process observed by direct monitoring during large-scale biaxial rock friction experiments. *Tectonophysics*, *733*, 182 - 192. Retrieved from `http://www.sciencedirect.com/science/article/pii/S0040195117305267` (Physics of Earthquake Rupture Propagation)

doi: https://doi.org/10.1016/j.tecto.2017.12.023

Galvez, P., Dalguer, L. A., Ampuero, J. P., & Giardini, D. (2016). Rupture Reactivation during the 2011 Mw 9.0 Tohoku Earthquake: Dynamic Rupture and Ground-Motion Simulations. *Bulletin of the Seismological Society of America*, *106*(3), 819. Retrieved from `http://dx.doi.org/10.1785/0120150153` doi: 10.1785/0120150153

Goebel, T. H. W., Schorlemmer, D., Becker, T. W., Dresen, G., & Sammis, C. G. (2013, September). Acoustic emissions document stress changes over many seismic cycles in stick-slip experiments. *Geophys. Res. Lett.*, *40*(10), 2049–2054. Retrieved from `https://doi.org/10.1002/grl.50507` doi: 10.1002/grl.50507

Goldberg, R., Siman-Tov, S., & Emmanuel, S. (2016). Weathering resistance of carbonate fault mirrors promotes rupture localization. *Geophysical Research Letters*, *43*(7), 3105–3111. Retrieved from `http://dx.doi.org/10.1002/2016GL067788` (2016GL067788) doi: 10.1002/2016GL067788

Gonzalez, R. C., Woods, R., & Eddins, S. L. (2009). *Digital Image Processing Using MATLAB*. Gatesmark Publishing.

Greenwood, J. A., & Williamson, J. B. P. (1966). Contact of Nominally Flat Surfaces. *Proceedings of the Royal Society of London A*, *295*(1442), 300–319. doi: 10.1098/rspa.1966.0242

Gulia, L., Tormann, T., Wiemer, S., Herrmann, M., & Seif, S. (2016). Short-term probabilistic earthquake risk assessment considering time-dependent b values. *Geophysical Research Letters*, *43*(3), 1100–1108. Retrieved from `http://dx.doi.org/10.1002/2015GL066686` (2015GL066686) doi: 10.1002/2015GL066686

Gulia, L., & Wiemer, S. (2019). Real–time discrimination of earthquake foreshocks and aftershocks. *Nature*, *574*, 193–199.

He, D., Zhou, P., Yan, Y., Kang, R., & Guo, D. (2017). Nonlinear Compression Behavior of the Grooved Polishing Pad: A Model and Its Validation. *ECS Journal of Solid State Science and Technology*, *6*(4), 178–183.

Heaton, T. H. (1990). Evidence for and implications of self-healing pulses of slip in earthquake rupture. *Physics of the Earth and Planetary Interiors*, *64*(1), 1–20. Retrieved from `http://www.sciencedirect.com/science/article/pii/003192019090002F` doi: http://dx.doi.org/10.1016/0031-9201(90)90002-F

Hillers, G., Mai, P. M., Ben-Zion, Y., & Ampuero, J.-P. (2007, 05). Statistical properties of seismicity of fault zones at different evolutionary stages. *Geophysical Jour-*

nal International, *169*(2), 515–533. Retrieved from https://doi.org/10.1111/j.1365-246X.2006.03275.x doi: 10.1111/j.1365-246X.2006.03275.x

Horowitz, F. G., & Ruina, A. (1989). Slip patterns in a spatially homogeneous fault model. *Journal of Geophysical Research: Solid Earth*, *94*(B8), 10279–10298. Retrieved from https://agupubs.onlinelibrary.wiley.com/doi/abs/10.1029/JB094iB08p10279 doi: 10.1029/JB094iB08p10279

Hu, S., Huang, W., Shi, X., Peng, Z., & Liu, X. (2019a, June). Bi-fractal feature of bi-Gaussian stratified surfaces. *Tribology International*, *134*, 427–434. Retrieved from http://www.sciencedirect.com/science/article/pii/S0301679X19300854

Hu, S., Huang, W., Shi, X., Peng, Z., & Liu, X. (2019b, March). Mechanism of bi-gaussian surface topographies on generating acoustic emissions under a sliding friction. *Tribology International*, *131*, 64–72. Retrieved from http://www.sciencedirect.com/science/article/pii/S0301679X18304961

Ide, S. (2019). Frequent observations of identical onsets of large and small earthquakes. *Nature*, *573*, 112–116.

Ide, S., & Aochi, H. (2005). Earthquakes as multiscale dynamic ruptures with heterogeneous fracture surface energy. *Journal of Geophysical Research: Solid Earth*, *110*(B11), n/a–n/a. Retrieved from http://dx.doi.org/10.1029/2004JB003591 doi: 10.1029/2004JB003591

Iio, Y. (1995). Observations of the slow initial phase generated by microearthquakes: Implications for earthquake nucleation and propagation. *Journal of Geophysical Research*, *100*(B8), 15333–15349. doi: 10.1029/95JB01150

Johnson, K. L. (1985). *Contact Mechanics*. Cambridge University Press.

Kammer, D. S., Radiguet, M., Ampuero, J.-P., & Molinari, J.-F. (2015, Jan 23). Linear Elastic Fracture Mechanics Predicts the Propagation Distance of Frictional Slip. *Tribology Letters*, *57*(3), 23. Retrieved from https://doi.org/10.1007/s11249-014-0451-8 doi: 10.1007/s11249-014-0451-8

Kammer, D. S., Yastrebov, V. A., Spijker, P., & Molinari, J.-F. (2012, Oct 01). On the Propagation of Slip Fronts at Frictional Interfaces. *Tribology Letters*, *48*(1), 27–32. Retrieved from https://doi.org/10.1007/s11249-012-9920-0 doi: 10.1007/s11249-012-9920-0

Kaneko, Y., & Ampuero, J.-P. (2011). A mechanism for preseismic steady rupture fronts observed in laboratory experiments. *Geophysical Research Letters*, *38*(21). doi: 10

.1029/2011GL049953

Kaneko, Y., Avouac, J.-P., & Lapusta, N. (2010, May). Towards inferring earthquake patterns from geodetic observations of interseismic coupling. *Nature Geoscience*, *3*(5), 363–369. Retrieved from `https://doi.org/10.1038/ngeo843`

Kaneko, Y., Nielsen, S. B., & Carpenter, B. M. (2016). The onset of laboratory earthquakes explained by nucleating rupture on a rate-and-state fault. *Journal of Geophysical Research: Solid Earth*, *121*(8), 6071–6091. doi: 10.1002/2016JB013143

Kaneko, Y., & Shearer, P. M. (2015). Variability of seismic source spectra, estimated stress drop, and radiated energy, derived from cohesive-zone models of symmetrical and asymmetrical circular and elliptical ruptures. *Journal of Geophysical Research: Solid Earth*, *120*(2), 1053–1079. Retrieved from `https://agupubs.onlinelibrary.wiley.com/doi/abs/10.1002/2014JB011642` doi: 10.1002/2014JB011642

Kato, A., Fukuda, J., Kumazawa, T., & Nakagawa, S. (2016). Accelerated nucleation of the 2014 Iquique, Chile Mw 8.2 Earthquake. *Scientific Reports*, *6*(24792). doi: doi:10.1038/srep24792

Kato, A., Obara, K., Igarashi, T., Hiroshi, T., Nakagawa, S., & Hirata, N. (2012). Propagation of Slow Slip Leading Up to the 2011 Mw 9.0 Tohoku-Oki Earthquake. *Science*, *335*, 705–708.

Kato, N. (2003). Repeating Slip Events at a Circular Asperity: Numerical Simulation with a Rate- and State-Dependent Friction Law. *Bull. Earthq. Res. Inst. Univ. Tokyo*, *78*, 151–166.

Ke, C.-Y., McLaskey, G. C., & Kammer, D. S. (2018). Rupture Termination in Laboratory-Generated Earthquakes. *Geophysical Research Letters*, *45*(23), 12,784–12,792. doi: 10.1029/2018GL080492

Kirkpatrick, J. D., & Brodsky, E. E. (2014). Slickenline orientations as a record of fault rock rheology. *Earth and Planetary Science Letters*, *408*, 24–34. doi: http://dx.doi.org/10.1016/j.epsl.2014.09.040

Kirkpatrick, J. D., Rowe, C. D., White, J. C., & Brodsky, E. E. (2013). Silica gel formation during fault slip: Evidence from the rock record. *Geology*, *41*(9), 1015–1018. Retrieved from `https://doi.org/10.1130/G34483.1`

Latour, S., Schubnel, A., Nielsen, S., Madariaga, R., & Vinciguerra, S. (2013). Characterization of nucleation during laboratory earthquakes. *Geophysical Research Letters*, *40*(19), 5064–5069. doi: 10.1002/grl.50974

Leefe, S. E., Dowson, D., Taylor, C. M., Childs, T. H. C., Dalmaz, G., Berthier, Y., ... Lubrecht, A. A. (1998, January). "Bi-Gaussian" representation of worn surface topography in elastic contact problems. In *Tribology series* (Vol. 34, pp. 281–290). Elsevier. Retrieved from http://www.sciencedirect.com/science/article/pii/S0167892298800837

Luo, Y., Ampuero, J. P., Galvez, P., van den Ende, M., & Idini, B. (2017). QDYN: a Quasi-DYNamic earthquake simulator (v1.1) [Computer software manual]. doi: 10.5281/zenodo.322459

Ma, S., Ma, J., & Liu, L. (2002). Experimental evidence for seismic nucleation phase. *Chin. Sci. Bull.*, *47*, 769–773. doi: https://doi.org/10.1360/02tb9174

Madariaga, R. (1976). Dynamics of an expanding circular fault. *Bulletin of the Seismological Society of America*, *66*(3), 639. Retrieved from http://dx.doi.org/

Maegawa, S., Suzuki, A., & Nakano, K. (2010, Jun 01). Precursors of Global Slip in a Longitudinal Line Contact Under Non-Uniform Normal Loading. *Tribology Letters*, *38*(3), 313–323. Retrieved from https://doi.org/10.1007/s11249-010-9611-7 doi: 10.1007/s11249-010-9611-7

Mai, P. M., & Beroza, G. C. (2002). A spatial random field model to characterize complexity in earthquake slip. *Journal of Geophysical Research: Solid Earth*, *107*(B11), 2308. Retrieved from http://dx.doi.org/10.1029/2001JB000588 doi: 10.1029/2001JB000588

Mai, P. M., Galis, M., Thingbaijam, K. K. S., Vyas, J. C., & Dunham, E. M. (2018). Accounting for Fault Roughness in Pseudo-Dynamic Ground-Motion Simulations. In L. A. Dalguer, Y. Fukushima, K. Irikura, & C. Wu (Eds.), *Best practices in physics-based fault rupture models for seismic hazard assessment of nuclear installations* (pp. 95–126). Cham: Springer International Publishing. Retrieved from https://doi.org/10.1007/978-3-319-72709-7_7 doi: 10.1007/978-3-319-72709-7_7

Mai, P. M., Somerville, P., Pitarka, A., Dalguer, L., Song, S., Beroza, G., ... Irikura, K. (2006). On Scaling of Fracture Energy and Stress Drop in Dynamic Rupture Models: Consequences for Near-Source Ground-Motions. In *Earthquakes: Radiated energy and the physics of faulting* (pp. 283–293). American Geophysical Union (AGU). Retrieved from https://agupubs.onlinelibrary.wiley.com/doi/abs/10.1029/170GM28 doi: 10.1029/170GM28

Marone, C., & Cox, S. J. D. (1994). Scaling of rock friction constitutive parameters: The

effects of surface roughness and cumulative offset on friction of gabbro. *Pure and Applied Geophysics*, *143*(1-3), 359–385. doi: 10.1007/BF00874335

McGuire, J. J., & Kaneko, Y. (2018). Directly estimating earthquake rupture area using second moments to reduce the uncertainty in stress drop. *Geophysical Journal International*, *214*(3), 2224–2235. Retrieved from http://dx.doi.org/10.1093/gji/ggy201 doi: 10.1093/gji/ggy201

McLaskey, G. C. (2019). Earthquake Initiation From Laboratory Observations and Implications for Foreshocks. *Journal of Geophysical Research: Solid Earth*, *124*(12), 12882-12904. Retrieved from https://agupubs.onlinelibrary.wiley.com/doi/abs/10.1029/2019JB018363 doi: 10.1029/2019JB018363

McLaskey, G. C., & Kilgore, B. D. (2013). Foreshocks during the nucleation of stick-slip instability. *Journal of Geophysical Research*, *118*(6), 2982–2997. doi: 10.1002/jgrb.50232

McLaskey, G. C., Kilgore, B. D., Lockner, D. A., & Beeler, N. M. (2014). Laboratory Generated M -6 Earthquakes. *Pure and Applied Geophysics*. doi: 10.1007/s00024-013-0772-9

McLaskey, G. C., & Lockner, D. A. (2014). Preslip and cascade processes initiating laboratory stick slip. *Journal of Geophysical Research: Solid Earth*, *119*(8), 6323–6336. Retrieved from http://dx.doi.org/10.1002/2014JB011220 doi: 10.1002/2014JB011220

Meier, M.-A., Heaton, T., & Clinton, J. (2016). Evidence for universal earthquake rupture initiation behavior. *Geophysical Research Letters*, *43*(15), 7991–7996. doi: 10.1002/2016GL070081

Mignan, A. (2012). Functional shape of the earthquake frequency-magnitude distribution and completeness magnitude. *Journal of Geophysical Research: Solid Earth*, *117*(B8). Retrieved from https://agupubs.onlinelibrary.wiley.com/doi/abs/10.1029/2012JB009347 doi: 10.1029/2012JB009347

Mignan, A. (2014). The debate on the prognostic value of earthquake foreshocks: A meta-analysis. *Scientific Reports*, *4*, 4099.

Mignan, A. (2020). Asymmetric Laplace Mixture Modelling of Incomplete Power-Law Distributions: Application to 'Seismicity Vision'. In K. Arai & S. Kapoor (Eds.), *Advances in computer vision* (pp. 30–43). Cham: Springer International Publishing.

Mogi, K. (1963). Some Discussions on Aftershocks, Foreshocks and Earthquake Swarms:

1267 the Fracture of a Semi-infinite Body Caused by an Inner Stress Origin and Its Relation
1268 to the Earthquake Phenomena (Third Paper). *Bulletin of the Earthquake Research*
1269 *Institute*, *41*, 615–658.

1270 Mogi, K. (1985). *Earthquake prediction*. Academic Press Japan.

1271 Nadeau, R. M., Antolik, M., Johnson, P. A., Foxall, W., & McEvilly, T. V. (1994). Seis-
1272 mological studies at Parkfield III: Microearthquake clusters in the study of fault-zone
1273 dynamics. *Bulletin of the Seismological Society of America*, *84*(2), 247–263.

1274 Nadeau, R. M., & McEvilly, T. V. (1999). Fault Slip Rates at Depth from Recurrence
1275 Intervals of Repeating Microearthquakes. *Science*, *285*(5428), 718–721. doi: 10.1126/
1276 science.285.5428.718

1277 Nielsen, S., Taddeucci, J., & Vinciguerra, S. (2010). Experimental observation of stick-slip
1278 instability fronts. *Geophysical Journal International*, *180*(2), 697–702. doi: 10.1111/
1279 j.1365-246X.2009.04444.x

1280 Noda, H., Nakatani, M., & Hori, T. (2013). Large nucleation before large earthquakes is
1281 sometimes skipped due to cascade-up – Implications from a rate and state simulation
1282 of faults with hierarchical asperities. *Journal of Geophysical Research: Solid Earth*,
1283 *118*(6), 2924–2952. Retrieved from `https://agupubs.onlinelibrary.wiley.com/`
1284 `doi/abs/10.1002/jgrb.50211` doi: 10.1002/jgrb.50211

1285 Obara, K., & Kato, A. (2016). Connecting slow earthquakes to huge earthquakes. *Science*,
1286 *353*(6296), 253–257. doi: 10.1126/science.aaf1512

1287 Ohnaka, M. (1992). Earthquake source nucleation: A physical model for short-term pre-
1288 cursors. *Tectonophysics*, *211*(1-4), 149–178. doi: dx.doi.org/10.1016/0040-1951(92)
1289 90057-D

1290 Ohnaka, M., & Shen, L. F. (1999). Scaling of the shear rupture process from nucleation to
1291 dynamic propagation: Implications of geometric irregularity of the rupturing surfaces.
1292 *Journal of Geophysical Research*, *104*(B1), 817–844. doi: 10.1029/1998JB900007

1293 Okubo, P. G., & Dieterich, J. H. (1984). Effects of physical fault properties on frictional
1294 instabilities produced on simulated faults. *Journal of Geophysical Research*, *89*(B7),
1295 5817–5827. doi: 10.1029/JB089iB07p05817

1296 Okuda, T., & Ide, S. (2018a). Hierarchical rupture growth evidenced by the initial seismic
1297 waveforms. *Nature Comunications*, *9*(3714).

1298 Okuda, T., & Ide, S. (2018b, August). Streak and hierarchical structures of the Tohoku-
1299 Hokkaido subduction zone plate boundary. *Earth, Planets and Space*, *70*(1), 132.

Retrieved from https://doi.org/10.1186/s40623-018-0903-8

Ozawa, S. W., Hatano, T., & Kame, N. (2019). Longer Migration and Spontaneous Decay of Aseismic Slip Pulse Caused by Fault Roughness. *Geophysical Research Letters*, *46*(2), 636–643. doi: 10.1029/2018GL081465

Passelègue, F. X., Latour, S., Schubnel, A., Nielsen, S., Bhat, H. S., & Madariaga, R. (2017). Influence of Fault Strength on Precursory Processes During Laboratory Earthquakes. In *Fault zone dynamic processes* (pp. 229–242). American Geophysical Union (AGU). Retrieved from https://agupubs.onlinelibrary.wiley.com/doi/abs/10.1002/9781119156895.ch12 doi: 10.1002/9781119156895.ch12

Pawlus, P. (2008, March). Simulation of stratified surface topographies. *Wear*, *264*(5), 457–463. Retrieved from http://www.sciencedirect.com/science/article/pii/S0043164807002062

Persson, B. N. J. (2006). Contact mechanics for randomly rough surfaces. *Surface Science Reports*, *61*(4), 201–227. doi: 10.1016/j.surfrep.2006.04.001

Pluymakers, A., & Røyne, A. (2017, October). Nanograin formation and reaction-induced fracturing due to decarbonation: Implications for the microstructures of fault mirrors. *Earth and Planetary Science Letters*, *476*, 59–68. Retrieved from http://www.sciencedirect.com/science/article/pii/S0012821X17304387

Power, W. L., & Tullis, T. E. (1991). Euclidean and fractal models for the description of rock surface roughness. *Journal of Geophysical Research*, *96*(B1), 415–424. doi: 10.1029/90JB02107

Pozzi, G., De Paola, N., Nielsen, S. B., Holdsworth, R. E., & Bowen, L. (2018). A new interpretation for the nature and significance of mirror-like surfaces in experimental carbonate-hosted seismic faults. *Geology*, *46*(7), 583. doi: 10.1130/G40197.1

Ranjith, K., & Rice, J. R. (1999). Stability of quasi-static slip in a single degree of freedom elastic system with rate and state dependent friction. *Journal of the Mechanics and Physics of Solids*, *47*(6), 1207–1218. Retrieved from http://www.sciencedirect.com/science/article/pii/S0022509698001136 doi: https://doi.org/10.1016/S0022-5096(98)00113-6

Renard, F., Voisin, C., Marsan, D., & Schmittbuhl, J. (2006, August). High resolution 3D laser scanner measurements of a strike-slip fault quantify its morphological anisotropy at all scales. *Geophysical Research Letters*, *33*(4), L04305. Retrieved from https://doi.org/10.1029/2005GL025038 doi: 10.1029/2005gl025038

Rice, J. R. (1993). Spatio-temporal complexity of slip on a fault. *Journal of Geophysical Research: Solid Earth*, *98*(B6), 9885–9907. doi: 10.1029/93JB00191

Roeloffs, E. A. (2006). Evidence for aseismic deformation rate changes prior to earthquakes. *Annual Review of Earth and Planetary Sciences*, *34*(1), 591-627. Retrieved from `https://doi.org/10.1146/annurev.earth.34.031405.124947` doi: 10.1146/annurev.earth.34.031405.124947

Rubin, A. M., & Ampuero, J. P. (2005). Earthquake nucleation on (aging) rate and state faults. *Journal of Geophysical Research: Solid Earth*, *110*(B11), n/a–n/a. Retrieved from `http://dx.doi.org/10.1029/2005JB003686` doi: 10.1029/2005JB003686

Rubinstein, S. M., Cohen, G., & Fineberg, J. (2004). Detachment fronts and the onset of dynamic friction. *Nature*, *430*, 1005–1009. doi: 10.1038/nature02830

Rubinstein, S. M., Shay, M., Cohen, G., & Fineberg, J. (2006). Crack-like processes governing the onset of frictional slip. *International Journal of Fracture*, *140*(1-4), 201–212. doi: 10.1007/s10704-006-0049-8

Ruina, A. (1983). Slip instability and state variable friction laws. *Journal of Geophysical Research*, *88*(B12), 10,359–10,370. doi: 10.1029/JB088iB12p10359

Ruiz, S., Metois, M., Fuenzalida, A., Ruiz, J., Leyton, F., Grandin, R., ... Campos, J. (2014). Intense foreshocks and a slow slip event preceded the 2014 Iquique Mw 8.1 earthquake. *Science*, *345*(6201), 1165–1169. Retrieved from `http://www.sciencemag.org/content/345/6201/1165.abstract` doi: 10.1126/science.1256074

Schmittbuhl, J., Chambon, G., Hansen, A., & Bouchon, M. (2006). Are stress distributions along faults the signature of asperity squeeze? *Geophysical Research Letters*, *33*(13), L13307.

Schmittbuhl, J., Vilotte, J.-P., & Roux, S. (1995, Jan). Reliability of self-affine measurements. *Phys. Rev. E*, *51*, 131–147. Retrieved from `https://link.aps.org/doi/10.1103/PhysRevE.51.131` doi: 10.1103/PhysRevE.51.131

Scholz, C. H. (1997, 08). Size distributions for large and small earthquakes. *Bulletin of the Seismological Society of America*, *87*(4), 1074-1077.

Scholz, C. H. (2002). *The Mechanics of Earthquakes and Faulting* (2nd ed.). UK: Cambridge University Press.

Scholz, C. H., & Aviles, C. A. (1986). The Fractal Geometry of Faults and Faulting. In *Earthquake source mechanics* (pp. 147–155). American Geophysical Union (AGU). doi: 10.1029/GM037p0147

Seif, S., Zechar, J. D., Mignan, S., A.and Nandan, & Wiemer, S. (2018, 12). Foreshocks and Their Potential Deviation from General Seismicity. *Bulletin of the Seismological Society of America*, *109*(1), 1-18. Retrieved from https://doi.org/10.1785/0120170188 doi: 10.1785/0120170188

Selvadurai, P. A. (2015). *Laboratory studies of frictional sliding and the implications of precursory seismicity* (phdthesis, Univerity of California, Berkeley). Retrieved from https://escholarship.org/uc/item/4xm835kb

Selvadurai, P. A. (2019). Laboratory insight into seismic estimates of energy partitioning during dynamic rupture: An observable scaling breakdown. *Journal of Geophysical Research: Solid Earth*.

Selvadurai, P. A., & Glaser, S. D. (2015a). Laboratory-developed Contact Models Controlling Instability on Frictional Faults. *Journal of Geophysical Research*, *120*(6), 4208–4236. doi: 10.1002/2014JB011690

Selvadurai, P. A., & Glaser, S. D. (2015b). Novel Monitoring Techniques for Characterizing Frictional Interfaces in the Laboratory. *Sensors*, *15*(5), 9791–9814. doi: 10.3390/s150509791

Selvadurai, P. A., & Glaser, S. D. (2017). Asperity generation and its relationship to seismicity on a planar fault: A laboratory simulation. *Geophysical Journal International*, *208*, 1009–1025. doi: doi:10.1093/gji/ggw439

Selvadurai, P. A., Glaser, S. D., & Parker, J. M. (2017). On factors controlling precursor slip fronts in the laboratory and their relation to slow slip events in nature. *Geophysical Research Letters*, *44*. Retrieved from http://dx.doi.org/10.1002/2017GL072538 doi: 10.1002/2017GL072538

Shirzaei, M., & Bürgmann, R. (2013). Time-dependent model of creep on the Hayward fault from joint inversion of 18 years of InSAR and surface creep data. *Journal of Geophysical Research*, *118*, 1733–1746. doi: 10.1002/jgrb.50149

Siman-Tov, S., Aharonov, E., Boneh, Y., & Reches, Z. (2015). Fault mirrors along carbonate faults: Formation and destruction during shear experiments. *Earth and Planetary Science Letters*, *430*, 367–376. Retrieved from http://www.sciencedirect.com/science/article/pii/S0012821X15005579 doi: http://doi.org/10.1016/j.epsl.2015.08.031

Siman-Tov, S., Aharonov, E., Sagy, A., & Emmanuel, S. (2013). Nanograins form carbonate fault mirrors. *Geology*, *41*(6), 703–706.

Siman-Tov, S., Stock, G. M., Brodsky, E. E., & White, J. C. (2017). The coating layer of glacial polish. *Geology*, *45*(11), 987–990. Retrieved from https://doi.org/10.1130/G39281.1

Socquet, A., Valdes, J. P., Jara, J., Cotton, F., Walpersdorf, A., Cotte, N., ... Norabuena, E. (2017). An 8 month slow slip event triggers progressive nucleation of the 2014 Chile megathrust. *Geophysical Research Letters*, *44*(9), 4046–4053. doi: 10.1002/2017GL073023

Svetlizky, I., & Fineberg, J. (2014). Classical shear cracks drive the onset of dry frictional motion. *Nature*, *509*, 205–209.

Tal, Y., Hager, B. H., & Ampuero, J. P. (2018). The Effects of Fault Roughness on the Earthquake Nucleation Process. *Journal of Geophysical Research: Solid Earth*, *123*(1), 437–456. doi: 10.1002/2017JB014746

Tinti, E., Spudich, P., & Cocco, M. (2005). Earthquake fracture energy inferred from kinematic rupture models on extended faults. *Journal of Geophysical Research: Solid Earth*, *110*(B12), n/a–n/a. Retrieved from http://dx.doi.org/10.1029/2005JB003644 (B12303) doi: 10.1029/2005JB003644

Tisato, N., Di Toro, G., De Rossi, N., Quaresimin, M., & Candela, T. (2012). Experimental investigation of flash weakening in limestone. *Journal of Structural Geology*, *38*, 183 - 199. Retrieved from http://www.sciencedirect.com/science/article/pii/S0191814111002057 (Physico-Chemical Processes in Seismic Faults) doi: https://doi.org/10.1016/j.jsg.2011.11.017

Tormann, T., Enescu, B., Woessner, J., & Wiemer, S. (2015). Randomness of megathrust earthquakes implied by rapid stress recovery after the Japan earthquake. *Nature Geoscience*, *8*, 152–158.

Tormann, T., Wiemer, S., & Mignan, A. (2014). Systematic survey of high-resolution b value imaging along Californian faults: Inference on asperities. *Journal of Geophysical Research: Solid Earth*, *119*(3), 2029–2054. Retrieved from http://dx.doi.org/10.1002/2013JB010867 doi: 10.1002/2013JB010867

Trømborg, J., Scheibert, J., Amundsen, D. S., Thøgersen, K., & Malthe-Sørenssen, A. (2011). Transition from static to kinetic friction: Insights from a 2D model. *Physical Review Letters*, *107*, 074301.

Uchida, N. (2019). Detection of repeating earthquakes and their application in characterizing slow fault slip. *Progress in Earth and Planetary Science*, *6*(40). Retrieved from

https://doi.org/10.1186/s40645-019-0284-z

Verberne, B. A., Plumper, O., & Spiers, C. J. (2019). Nanocrystalline Principal Slip Zones and Their Role in Controlling Crustal Fault Rheology. *Minerals*, *9*, 328.

Wang, K., & Bilek, S. L. (2014, January). Invited review paper: Fault creep caused by subduction of rough seafloor relief. *Tectonophysics*, *610*, 1–24. Retrieved from http://www.sciencedirect.com/science/article/pii/S0040195113006896

Wiemer, S., & Wyss, M. (2002). Mapping spatial variability of the frequency-magnitude distribution of earthquakes. In R. Dmowska & B. Saltzman (Eds.), (Vol. 45, p. 259 - V). Elsevier. Retrieved from http://www.sciencedirect.com/science/article/pii/S0065268702800073 doi: https://doi.org/10.1016/S0065-2687(02)80007-3

Yoshioka, N. (1997). A review of the micromechanical approach to the physics of contacting surfaces. *Tectonophysics*, *277*(1), 29–40. Retrieved from http://www.sciencedirect.com/science/article/pii/S0040195197000760 (Earthquake Generation Processes: Environmental Aspects and Physical Modelling) doi: https://doi.org/10.1016/S0040-1951(97)00076-0

Yoshioka, N., & Iwasa, K. (1996). The characteristic displacement in rate and state-dependent friction from a micromechanical point of view. *Pure and Applied Geophysics*, *147*(3), 433–453. doi: 10.1007/BF00878837

Zhuo, Y.-Q., Guo, Y., Chen, S., Ji, Y., & Ma, J. (2018). Laboratory Observations of Linkage of Preslip Zones Prior to Stick-Slip Instability. *Entropy*, *20*, 629.

Zhuo, Y.-Q., Liu, P., Chen, S., Guo, Y., & Ma, J. (2018). Laboratory observations of tremor-like events generated during preslip. *Geophysical Research Letters*, *45*(14), 6926-6934. Retrieved from https://agupubs.onlinelibrary.wiley.com/doi/abs/10.1029/2018GL079201 doi: 10.1029/2018GL079201